An Exploration of Electron-Excited Surface Plasmon Resonance For Use In Biosensor Applications

A Thesis
Presented to
The Academic Faculty

by

Adam D. Wathen

In Partial Fulfillment
of the Requirements for the Degree
Master of Science in Electrical Engineering

School of Electrical and Computer Engineering
Georgia Institute of Technology
April 2004

An Exploration of Electron-Excited Surface Plasmon Resonance For Use In Biosensor Applications

Approved by:

Professor William D. Hunt, Committee Chair, Advisor

Professor David Hertling, Committee Member

Professor John Buck, Committee Member

Date Approved: 12 April, 2004

ACKNOWLEDGEMENTS

I would like to take this opportunity to express my sincere gratitude to everyone who assisted in the completion of this thesis, both directly and indirectly. Foremost, I would like to thank my advisor, Dr. William Hunt for allowing me this research opportunity and for his continuous support and direction. In addition, I would like to thank Dr. David Hertling and Dr. John Buck[1] for serving as committee members. Thanks is in order for Dr. Z.L. Wang in the Materials Science department here at Georgia Tech for his assistance regarding the excitation probability calculations.

Special recognition is in order for everyone I worked with at Sandia National Laboratories: Dr. Stephen Cassalnuovo, Dr. Paul Kotula, Dr. Thomas Headley, Dr. Darren Branch, Dr. Andrew Boal, Mr. Ron Goeke, all of whom contributed significant technical expertise and assistance. Mrs. Monica Manginell, my former temporary office mate at Sandia, also deserves thanks for helping to make doing office work actually fun. I would also like to thank Dr. Peter Feibelman of SNL and Dr. Javier Aizpurua of the Donostia International Physics Center for some engaging private conversation regarding this work.

I would like to thank my colleagues here at Georgia Tech: Desmond Stubbs, Sang-Hun Lee, Anthony Dickherber, Chris Corso, Frank Pyrtle and Kimsey Pollard. Even though I did not actually work very closely with many of you, you all made it more enjoyable nonetheless. In addition I would like to thank one of my students, Ryan Westafer, for his assistance regarding the FORTRAN program used for some calculations. Special thanks goes out to my roommates Sven Krasser and Michael Kettner for helping me solve some last-minute problems regarding LaTeX.

In addition to all who assisted with the technical aspects of this work, a substantial amount of encouraging support came from those closest to me. I would like to thank my

[1] I am especially grateful to Dr. Buck for his generosity in joining my committee at the very last minute. If it weren't for my entire committee's willingness to bend over backward for me so close to the submission deadline, I certainly would not have graduated on time.

friends here in Atlanta, Chicago, Purdue, and around the country for their encouraging words, repeated sanity checks and some good times[2] during the course of my studies here. Most importantly, I express my deepest appreciation and love to my family[3] whose never-ending support was, and always will be, essential to my success.

[2]For example, tailgating, fried turkeys, the Yukka, 'ruit, Tippy Toe, Grand Prix, Mardi Gras, Cancun, trivia Tuesdays, and ABC Fridays, just to name a few. Clearly there are too many to list.

[3]Of course, the only part of this thesis they will probably understand is this Acknowledgments section...and maybe the Table of Contents, but that is beside the point.

TABLE OF CONTENTS

ACKNOWLEDGEMENTS . . . . . **iii**

LIST OF TABLES . . . . . **vii**

LIST OF FIGURES . . . . . **viii**

SUMMARY . . . . . **x**

I INTRODUCTION **1**

1.1 A Brief Introduction to Plasmon Oscillations and Their Potential Use . . . 1

1.2 A General Overview of This Thesis 5

II EXPERIMENTAL WORK **7**

2.1 Preliminary Investigations 7

2.1.1 Surface Plasmons in the Scanning Electron Microscope 7

2.1.2 First Attempt At Reproducing SPR in a TEM 9

2.1.3 Some Structural Concerns of the Proposed Device 10

2.2 Sample Preparation 14

2.2.1 Gold Nanoparticle Samples 14

2.2.2 Fabrication and Application of Thin Gold Film Samples 18

2.2.3 Biology Used in Experimentation and Immobilization Protocols . . 19

2.2.4 Description of Electron Energy Loss Spectrum Collection Process . 21

III RESULTS **23**

3.1 EELS of Gold Samples 23

3.1.1 EELS of Plain Gold Films 25

3.1.2 EELS of Gold Film with Biology 27

3.2 EELS of Silicon Nitride Samples 29

3.2.1 EELS of Functionalized Silicon Nitride Samples Without Biology . 29

3.2.2 EELS From Silicon Nitride Samples With the Addition of Biology . 33

IV ANALYSIS OF RESULTS AND CONCLUSIONS **35**

4.1 Origination of Excitation Probability 35

4.2 Analysis of the Excitation Probabilities 41

4.3 Concluding Remarks 43

APPENDIX A — EXCITATION PROBABILITY FORTRAN PROGRAM 46

REFERENCES 53

LIST OF TABLES

Table 1 Tabulated surface currents due to varying acceleration voltages and angles of incidence 8

LIST OF FIGURES

Figure 1 Polarized dielectric medium (redrawn from [2]) 3

Figure 2 (left) Polarization vector in dielectric medium 2. (right) Bounded charge density and resulting electric field at interface of two dielectrics (redrawn from [2]) 3

Figure 3 200 mesh TEM grid. (Image provided by www.tedpella.com) 9

Figure 4 Magnification of Lacey Formvar TEM grid coating. (Image provided by www.tedpella.com) 9

Figure 5 Flat plate geometry 11

Figure 6 Example of hexagonal honeycomb structure 12

Figure 7 Multi-cell eSPR micro-array with nanotube emitters 13

Figure 8 Tilted 45 degree top (a) and cross-sectional (b) SEM images of a micro-cathode. (Pirio et, al [1]) 13

Figure 9 0.26μm diameter Latex suspended on a Lacey Support Film (Image provided by www.tedpella.com) 15

Figure 10 20 nm evaporated gold particles 15

Figure 11 20 nm evaporated gold particles magnified 16

Figure 12 5 nm particle aggregates 16

Figure 13 SEM image of a 100 nm Si_3N_4 membrane window grid (Image provided by www.2spi.com) 17

Figure 14 Diagram of Au particle monolayer on thiol groups 17

Figure 15 15nm gold film on lacey TEM grid 19

Figure 16 Low-loss region of EELS spectrum (Image provided in [15]) 21

Figure 17 Inner shell-loss region of EELS spectrum (Image provided in [15]) 21

Figure 18 EELS spectrum from 15nm gold film 24

Figure 19 Low-loss region of the EELS spectrum from 15nm gold film 24

Figure 20 Spectra from three 15nm gold samples 25

Figure 21 Derviatives of spectra from three 15nm gold samples 26

Figure 22 Derviatives of spectra from three 15nm gold samples 26

Figure 23 EELS from three 15nm gold films with varying BSA concentrations . . . 27

Figure 24 Derivatives of spectra from three 15nm gold films with varying BSA concentrations 27

Figure 25 Spectra of Si_3N_4 29
Figure 26 Derivatives of Si_3N_4 spectra 30
Figure 27 Spectra of Si_3N_4 plus an amine layer 30
Figure 28 Derivatives of Si_3N_4 plus amine spectra 31
Figure 29 Spectra of Si_3N_4 plus an amine layer and 10nm gold particles 32
Figure 30 Derivatives of Si_3N_4 plus amine spectra 32
Figure 31 Derivatives of collected spectra 32
Figure 32 Magnified derivatives of collected spectra 33
Figure 33 EELS spectra of Si_3N_4 with BSA 33
Figure 34 Derivatives of Si_3N_4 with BSA spectra 34
Figure 35 Schematic of momentum transfer 37
Figure 36 Dielectric function of gold 40
Figure 37 Volume and surface plasmon losses in gold 41
Figure 38 Total surface plasmon excitation probabilities 42
Figure 39 Total bulk plasmon excitation probabilities 42
Figure 40 Ratio of surface to bulk excitation probabilities 43
Figure 41 Total excitation probability in 15nm gold film 44

SUMMARY

Surface plasmon resonance (SPR) is a physical phenomenon that is not only of pure academic interest, but also has several wide-ranging applications. One of these applications is in various sensors. SPR using optical excitation is widely used in biosensor applications. These sensors are extremely sensitive, but have the tendency to be relatively large, expensive, and ignore the potentials of microelectronic technology.

SPR was first discovered in transmission electron microscopy. In this case, the excitation is a fast-moving electron impinging on a material. The goal of this research is to determine whether or not this electronic excitation can be harnessed in order to create a sensing device that will be comparable to the optical SPR devices, but will be significantly smaller, cheaper, and more portable. Chapter 1 introduces the concept of SPR and discusses some of the potential uses of it in sensors.

Chapter 2 discusses some preliminary research done on this topic. It was found that using scanning electron microscopy will not work to measure surface plasmons and that transmission electron microscopy (TEM) is required to measure these effects. Various metallic samples were fabricated for the TEM including those made from gold nanoparticles and a 15nm gold film. The goal of this project is to perform the preliminary research into creating a sensor that can detect various biological and chemical binding events. So, also in this chapter are the various biomolecule immobilization schemes used for applying DNA, BSA, and protein A to these gold samples.

Some research was done regarding the structure of a possible device as well, which is also discusses in Chapter 2. It is proposed that the device utilize vacuum microelectronic technology which required a vacuum well bounded by an extremely thin layer of gold as the sensing surface. It was found that it is possible to fabricate an array of 2μm wells with carbon nanotube electron emitters [1] and if a thin gold film could be applied over them, the result would be a two-dimensional array of independent sensors.

Chapters 3 and 4 cover the experimental and theoretical aspects of this project more deeply. In Chapter 3, data is presented from electron energy loss spectroscopy (EELS) which was performed on the samples described above. It is shown that due to the energy resolution of the EELS spectrometer and the fact that some of the samples may be getting destroyed in the TEM due to the prolonged illumination by the electron beam that the effects of biological binding events are inconclusive. Chapter 4 introduces electron energy loss theory in much greater detail than Chapter 1 and includes derivations of the excitation probability and the electron energy loss function. Theoretical calculations of the effects of surface plasmon excitations on the EELS spectrum are also included. It is shown that due to the high energy of the electron beam and the normally-incident trajectory that the surface effects are extremely small in the 15nm films used in the experimentation.

Chapter 4 also includes some closing remarks regarding the feasibility of using electronic excitation of SPR in a sensing device. It is hypothesized that in order to accomplish this goal, the only way to measure the surface plasmon effects is by measuring electron energy loss. This would mean that an entire EELS spectrometer may have to be shrunk to a microelectronic scale long before any attempt at a working device could even be considered. This is surely something that is potentially several years away from being realized.

CHAPTER I

INTRODUCTION

Surface plasmons are defined by Burstein et. al [2] as the electromagnetic modes that propagate like waves along the interface between two materials, but are evanescent in nature. These modes are typically induced by photon/electric-dipole coupling at the surface. This phenomena, also knows as surface plasmon resonance, is widely used in biosensor applications. These sensors, such as Texas Instruments' Spreeta system and Biacore's SPR biosensor, are extremely sensitive measuring devices but are relatively large, expensive, and do not take full advantage of microelectronic technology.

1.1 A Brief Introduction to Plasmon Oscillations and Their Potential Use

During the first half of the 20th century, there was an extensive amount of theoretical and experimental research being conducted to investigate characteristic energy losses by fast electrons passing through thin metal foils. Pines and Bohm [3] suggested that these energy losses are due to plasma oscillations or "plasmons" in the sea of conduction electrons. Generally speaking, this sea of conduction electrons, or the "electron gas" or "plasma" refers to bulk materials which have properties that allow the assumption of the conduction electrons acting as a free electron gas. Aluminum is a particularly good example of this type of metal. The electron gas is characterized by the dielectric function

$$\varepsilon(\mathbf{k},\omega) = 1 - \frac{\omega_p^2}{\omega(\omega + i/\tau)} \tag{1}$$

where ω_p is the characteristic plasma frequency of the material given by

$$\omega_p^2 = \frac{ne^2}{\varepsilon_0 m_e}, \tag{2}$$

such that n is the free electron density of the material, e is the electron charge, and m_e is the effective mass of an electron. τ accounts for the dissipative effects in the system. When

the electron gas is excited by an external source with a frequency equal to ω_p, and damping is negligible, it was shown that the electrons collectively oscillate in the material. This is sometimes referred to as a *bulk plasmon*.

Gabor [4] attempted to develop a theory to describe the energy loss characteristics of electrons passing through finite metal crystals. As Ritchie [5] points out, Gabor mistakenly assumed that the electric field is always zero at the surface of the crystal, which led to unrealistic results. Ritchie applied more realistic boundary conditions and calculated the electron interaction probability in extremely thin films. His work resulted in the prediction of *surface plasmons* and consequently pioneered a whole new field of interest in surface physics.

The surface plasmons are generally considered as charge density oscillations that propagate very close to the surface of a metal. The consequence of this charge density is that, since the normal components of the displacement vector due to the charges must be continuous, we arrive at the equation

$$\varepsilon_p(\omega) = -\varepsilon_d(\omega) \tag{3}$$

where $\varepsilon_p(\omega)$ is the dielectric function of a semi-infinite plasma electron gas and $\varepsilon_d(\omega)$ is that of the bounding dielectric.

Burstein et al. [2] further elaborated on the surface excitations at interfaces from an optical standpoint. In Figure 1, a bulk polarization vector of the form $\mathbf{P} = \mathbf{P}_0 e^{i(\omega t - kx)}$ propagates in an infinite dielectric medium 2 in the x direction. In infinite dielectric media, $\nabla \cdot \mathbf{P} = 0$ so there are no volume charges in the media and therefore no macroscopic electric field. A dielectric medium (medium 1) is placed normal to the polarization field. Due to the different materials on each side of the interface, a discontinuity appears in $\mathbf{P}$ and a surface charge density appears on the interface. It is important to note that this charge density is not a free charge density, as in a surplus or deficit of electrons. In viewing dielectric materials microscopically (Figure 1), it is clear that the net charge inside the material when it is placed in an electric field is zero. However, there is a "charge" on the surface which is either positive or negative. These charges are actually the nuclei and the electrons of each individual molecule in the material, respectively.

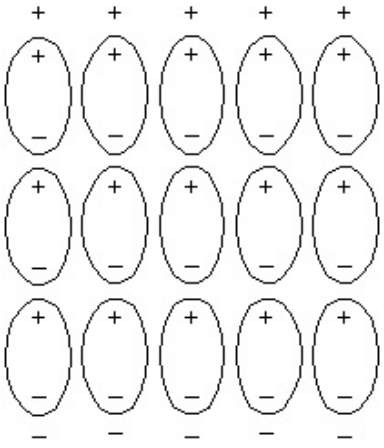

Figure 1: Polarized dielectric medium (redrawn from [2])

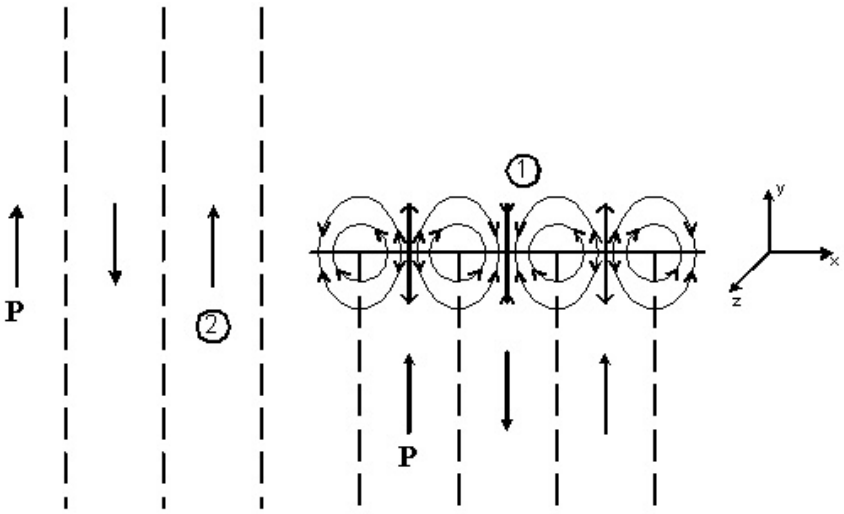

Figure 2: (left) Polarization vector in dielectric medium 2. (right) Bounded charge density and resulting electric field at interface of two dielectrics (redrawn from [2])

This new charge density creates a macroscopic electric field with x and y components only (Figure 2). This charge density is the only source of the electric field, since all other conditions in the materials are the same as in the previous case. The y components of the electric field at the interface (and at every point equidistant from it on both sides of the interface) are obviously of equal magnitude and of opposite sign.

Since polarized dielectrics give rise to this extra charge density, the divergence of the electric field must be modified to include its effect:

$$\nabla \cdot \mathbf{E} = \frac{1}{\epsilon_0}(\rho_v + \rho_b), \tag{4}$$

where ρ_b is the *bound* charge density induced by the polarization field. A property of the polarization vector is that $\nabla \cdot \mathbf{P} = -\rho_b$. Using this, the equation above becomes

$$\nabla \cdot (\epsilon_0 \mathbf{E} + \mathbf{P}) = \rho_v, \tag{5}$$

where ρ_v is the distribution of *free* charges in a medium. We can rewrite this equation as Eq. 3 simply by substituting $\mathbf{D}$ for $\epsilon_0 \mathbf{E} + \mathbf{P}$. Since Eq. 3 then only deals with *free* charges, and there are no free charges in the situations we are dealing with here, the condition for $\mathbf{D}$ becomes

$$D_{n1} = -D_{n2} \tag{6}$$

which results in

$$\epsilon_1(\omega) = -\epsilon_2(\omega). \tag{7}$$

The consequence of this somewhat strange result is that for charges to be "bound" at an interface, one of the permittivities must be negative. As noted previously, when an electromagnetic wave is incident upon a metallic surface, the permittivity of the metal depends on the frequency of the incoming wave. If the frequency is less than the plasma frequency, ω_p, the permittivity is then negative which creates these surface excitations. When these are coupled with incoming photons, the results are surface plasmons.

Substituting Equation 7 into Equation 1, neglecting damping, and solving for the resonant frequency of the surface wave yields

$$\omega_r = \frac{\omega_p}{\sqrt{1 + \varepsilon_d}}. \tag{8}$$

If the bounding material is a vacuum, then the resonant frequency is simply given by $\omega_p/\sqrt{2}$ and is consistent with Ritchie's [5] predicted result. However, if the bounding layer is a dielectric, the resonant frequency can be decreased significantly. As shown by Stern and Ferrell [6], if the dielectric is absorptive at the new resonance the dielectric constant, and hence the resonant frequency, will be complex. For small values of the imaginary part of the dielectric function, one can isolate the imaginary part of the resonant frequency to give the breadth of the resonance τ^{-1}. This is given by the equation

$$\tau^{-1} = \frac{\omega_r \varepsilon_i}{(1+\varepsilon_r)^{3/2}}, \tag{9}$$

with ε_i and ε_r being the imaginary and real parts of the dielectric function of the surrounding dielectric, respectively. As ε_i exceeds 1, the breadth of the resonance peak becomes so smeared across various energies that the effect can no longer be consider a collective oscillation. This clearly shows that the surface plasmon resonance (SPR) oscillations depend on the dielectric properties of the surrounding dielectric medium and this is precisely the phenomenon we would like to exploit in SPR sensing devices.

1.2 A General Overview of This Thesis

As stated previously, optical SPR sensors are relatively large, expensive, and do not take full advantage of microelectronic technology. A typical Biacore single SPR sensor system, including supporting electronics, can cost about $350,000. This system is extremely sensitive, but cost and the lack of portability make it only suitable in a laboratory environment. The goal of the proposed research is to advance the understanding of the physical principles behind electron beam excited surface plasmon resonance (eSPR) and determine the feasibility of its use in biosensor applications. Using electron microscopy imaging techniques such as scanning electron microscopy (SEM) and transmission electron microscopy (TEM), detection of surface plasmons on thin gold films with various biological coatings will provide data as to whether or not eSPR will be suitable as a biosensing modality.

Chapter 2 discusses the basic experimental procedure involved in this work. Included are descriptions of and results from the first experiments involving the SEM and the TEM

as well as some brainstorming on particular structural concerns having to do with an eventual device if one were to be fabricated in the future. The sample preparation procedures are also described including the fabrication and application of a very thin gold film and the immobilization schemes involved when using various biological coatings. The surface plasmons will be detected using Electron Energy Loss Spectroscopy (EELS) and this process is also briefly described.

Chapters 3 and 4 present the results of the experimentation and the analysis of those results. Chapter 3 includes EELS spectra collected from all of the various samples used throughout this work. Chapter 4 is a description of the physics and the mathematics of electron energy loss and attempts to solve, or at least explain, some of the problems that were encountered during the experimentation.

CHAPTER II

EXPERIMENTAL WORK

2.1 Preliminary Investigations

2.1.1 Surface Plasmons in the Scanning Electron Microscope

The first step in this research is to reproduce reported plasmon oscillations in thin gold films caused by electron microscopy techniques. Golstein [9] mentions that SPR can occur in SEM images. SEM is a relatively simple imaging modality to work with and therefore will be a starting point in the reproduction of the plasmons. The surface on which the experimentation will take place in the SEM is a 50nm vacuum evaporated gold film on a silicon wafer substrate. By adjusting the acceleration voltage and angle of incidence of the electron beam, plasmons should be able to be imaged in the form of black spots on the gold film due to the energy loss of the electrons inducing the plasmons. By quantifying the conditions needed to induce these plasmons, a basis for which to fabricate an eventual device is created.

Since SEM is a relatively simple imaging modality to experiment with, our first attempt to generate plasmons involved the use of a Hitachi S-800 FEG SEM provided by Dr. Z.L. Wang in the Materials Science and Engineering department here at Georgia Tech. The films used in the experiment were 50nm evaporated gold films. By changing the acceleration voltage and the angle of incidence of the electron beam inside the SEM, we hoped to generate and consequently image plasmons in the form of dark spots on the gold films. However, since the SEM available only allows for coarse incident angle adjustments and a relatively small accelerating voltage range to work with (only about 200eV-20keV), the imaging of the plasmons proved to be futile.

Since surface plasmons are defined in the literature to be the collective oscillation of free electrons on the surface of a material, we then hypothesized there to be an induced current on the surface of the metal. In order to capture and measure this current, we wire bonded

the gold film to the sample stage used to stabilize the sample inside the SEM. Contained in the SEM is a coaxial connector attached to the stage specifically for these types of measurements. One would think that if plasmons were indeed generated on the film that there would be an increase in the magnitude of the current on the surface. As shown in Table 1, for some combinations this is the case but there is no predictable pattern. However, there are several possible sources of error that may have arisen in these measurements.

Table 1: Tabulated surface currents due to varying acceleration voltages and angles of incidence

$\theta \setminus$ kV	6	8	10	12	14	16	18	20
0	0.025	0.15	0.31	0.54	0.87	1.3	1.6	1.9
5	0.036	0.17	0.32	0.57	0.92	1.3	1.7	2.0
10	0.046	0.18	0.33	0.57	0.92	1.3	1.65	2.0
15	0.05	0.18	0.33	0.57	0.85	1.3	1.6	2.05
20	0.063	0.18	0.34	0.60	0.85	1.3	1.65	2.05
25	0.063	0.18	0.32	0.58	0.83	1.25	1.6	2.0
30	0.052	0.15	0.3	0.5	0.83	1.2	1.5	2.0
35	0.012	0.09	0.22	0.43	0.7	1.1	1.35	2.0
40	n/a	n/a	0.1	0.27	0.53	0.9	1.15	1.7
45	n/a	n/a	0.08	0.25	0.47	0.8	1.05	1.4

First, there is no way to acquire data for all possible combinations of incident angle and acceleration voltage because the stage inside the SEM can only rotate a maximum of 45 degrees. This obviously prevents obtaining measurements from angles greater than 45 degrees. Second, since the SEM captures images using an electron beam, the currents we are measuring may, if fact, be those electrons hitting the stage itself, rather than plasmons on the gold. Yet another possible source of error is the DC ammeter used. Since the ammeter was analog, the degree of precision is, at best, two decimal places. A problem with this is that we are uncertain of the magnitude of the current induced by the plasmons on the film, if there is any at all. If the magnitude is on the order of picoamps or smaller, it will go unnoticed with this type of measurement. Also, since the ammeter can only measure DC currents, if the current induced by a plasmon contains several frequencies, again, we will not be able to measure it.

2.1.2 First Attempt At Reproducing SPR in a TEM

Since it was seen to be too difficult to obtain results using an SEM and the equipment available to us, we began work on the TEM method. So rather than using scattered electrons or induced currents on the films, we turned to analyzing transmitted electrons instead. Much research has been conducted on energy losses in scattered electrons from various materials, but Ruthemann [10] was the first to perform the same loss measurements on transmitted electrons through thin films. As stated earlier, our goal was to reproduce the spectrum for gold films, then determine what effect the additions of other materials on the films would have on the energy loss spectra. We used a Hitachi HF-2000 field emission gun (FEG) transmission electron microscope (TEM) (200kV) with a Gatan parallel-detection electron energy-loss spectrometer (PEELS) attached again provided by Dr. Wang to perform the measurements. We first evaporated gold films onto three lacey Formvar coated TEM sample support film grids provided by Ted Pella Inc. shown in Figures 3 and 4.

Figure 3: 200 mesh TEM grid. (Image provided by www.tedpella.com)

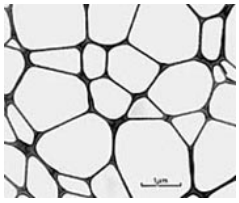

Figure 4: Magnification of Lacey Formvar TEM grid coating. (Image provided by www.tedpella.com)

Two had 50nm films and one had a 70nm film evaporated onto the Formvar coating. One of the 50nm films was then coated with a layer of antibodies (average height of 20nm).

We could then compare the spectra of the 70nm film and the antibody coated film to that of the plain thin gold film. The added thickness of the 70nm gold will certainly affect the resulting spectrum, as will the addition of the antibodies. The question we wanted answered, however, is if the spectrum change was due simply to the added thickness, or do the differing materials make significant changes in the spectra?

When the experiments were performed, we could not acquire any spectrum at all. Formvar thicknesses on the TEM grids are approximately 30-60nm by themselves. With the gold ranging from 50-70nm, the overall thickness is between 80-130nm. For the TEM to effectively image specimens, the thickness of the sample should be as thin as possible, i.e. no greater than 70nm. The thickness of the samples may have been too great for the TEM to work effectively. Another cause for this problem could be that the PEELS system used was not functioning properly, if at all. If the samples were too thick, the spectrum of the film would have been a flat line with a possible spike at a very high energy loss if any electrons penetrated through the film at all. We did achieve this characteristic flat curve from the PEELS system. The specimen was then removed entirely, which should result in a very large spike at the zero-loss mark on the spectrum with nothing else present but noise. Still, the obtained spectrum was flat everywhere, including the zero-loss mark thus giving no useful spectrum to analyze. Since we were unable to obtain any sort of spectrum at all, it was concluded that the PEELS system was not functioning properly.

2.1.3 Some Structural Concerns of the Proposed Device

Some of the structural problems of a potential device were also assessed prior to conducting the main part of this research. Looking ahead to the future design of the eSPR sensor utilizing vacuum microelectronics, it was determined that a thin layer of some supporting oxide covered with the metal film itself would be necessary for mechanical stability of the device. The electron source would be located inside of a well at vacuum pressure, which is why the addition of the oxide is needed to satisfy mechanical requirements. A 50nm gold film would simply tear under the pressure. With the need of this additional oxide layer, it needed to be determined if one could see through the oxide to the metal inside the SEM. Initial

experiments were done using SiO_2 sputtered over an arbitrarily thin aluminum layer. The films were tested by setting 30nm deep features in the aluminum layer prior to sputtering the oxide above. Both the maximum and minimum angular and voltage settings were successful in imaging the features below the SiO_2 layer. Of course, the limitations on the angular and power adjustments described above were still present. Nevertheless, the added oxide proved to be "transparent" to electrons and could make a good mechanically supporting layer for the eSPR device. Another solution we briefly examined was using silicon nitride as the supporting layer. Si_3N_4 is both strong enough to withstand the pressure difference and is transparent to electrons. In order to investigate this possibility, we modeled the Si_3N_4-metal layer as flat plate. Assume that the plate is rectangular with width a, height b, and thickness h (Figure 5). All sides are fixed and the deflection y is given by [11]

$$y = \frac{0.0284qa^4}{Eh^3\left[1 + 1.05(\frac{a}{b})^5\right]} \tag{10}$$

where q denotes the applied load and E is the modulus of elasticity. Using physical properties of Si_3N_4 provided by Cercom Inc., and assuming the structure to be square (a = b = 100μm), the required thicknesses of the film range from 1.45μm to about 3μm. This, however, does not account for structure failure. We learned from Dr. David McDowell in the Mechanical Engineering Department here at Georgia Tech that a circular film of radius 50μm under 1 ATM of pressure requires a 0.72μm thickness at failure. He also informed us that a safety factor of about 2-4 should be incorporated which makes an overall reasonable thickness of about 2-4μm. This result sounds promising, but trying to pass electrons through a layer of silicon nitride that thick may be difficult.

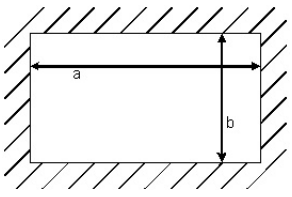

Figure 5: Flat plate geometry

Another proposed solution is actually a structural concept taken from nature. Honeybees construct their honeycombs by making a series of hexagonal cells (Figure 6). The reason for this geometry is that the hexagon allows for a large interior volume of the cell using a small amount of material to create the structure. In addition to the geometrical advantages of a hexagonal structure, it also provides significant structural integrity meaning that it can withstand considerable loads before failure occurs.

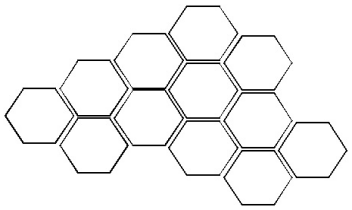

Figure 6: Example of hexagonal honeycomb structure

We propose replacing the uniform layer of Si_3N_4 under the metal film with a layer that is honeycomb in nature. This new geometry has several interesting consequences. One is that the amount of material used as the support layer is dramatically reduces. With the addition of the holes (honeycomb cells) in the layer, the electrons will not have to pass through several microns of material before interacting with the metal film. Also, the honeycomb geometry effectively divides the metal film into several cells. Exploiting this result, each cell can be used as its own sensor with an extremely small active surface area. As a result, this metal film could be used a 2-D array of eSPR sensors.

A diagram of the proposed 2-D array device is shown in Figure 7. As shown the device would consist of a matrix of small cells each with their own active gold sensing surface. Carbon nanotubes were briefly considered as the source of electrons in the device because of the high current density (as high as 1.2 A/cm^2) obtained using a relatively low accelerating voltage (less than 8 V/m in some cases) [12].

A solution to the problem of dividing the device into individual cells along with the fabrication of the carbon nanotube electron emitters was given by Pirio et. al [1]. They have developed a carbon nanotube field emission microcathode with an integrated gate electrode

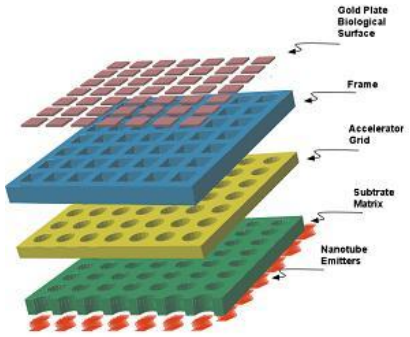

Figure 7: Multi-cell eSPR micro-array with nanotube emitters

(Figure 8). Each device is 2μm in diameter. The current density measured was 0.6mA/cm^2 using a 40 V acceleration voltage with a 0.5% duty cycle. Although not honeycomb in nature as described in the previous section, these circular devices could still achieve the same effect as what we desire for a large 2-D sensor grid.

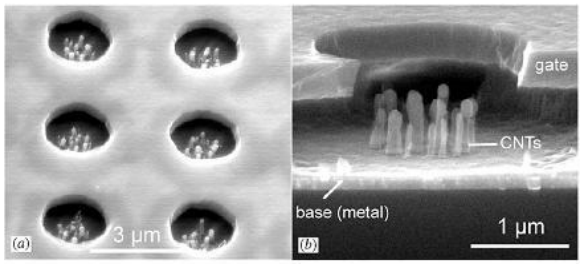

Figure 8: Tilted 45 degree top (a) and cross-sectional (b) SEM images of a microcathode. (Pirio et, al [1])

2.2 Sample Preparation

Since it was shown in the previous work that attempting to reproduce measurable plasmons in an SEM proved to be fruitless, the only other method available to us was the use of a TEM. As said before, Dr. Wang's TEM here at Georgia Tech was not functioning properly so my advisor, Dr. Hunt, referred me to some researchers at Sandia National Laboratories (SNL) in Albuquerque, New Mexico and was allowed limited access to their imaging equipment and labs. Under the direction of Dr. Steve Cassalnuovo, Dr. Thomas Headley, and Dr. Paul Kotula at SNL, I performed the rest of my TEM experimentation.

2.2.1 Gold Nanoparticle Samples

As stated perviously, the TEM grids with the gold evaporated on them used in the short experimentation at Georgia Tech were unsuitable for taking the EELS measurements we needed. So, in order to prevent wasting time at SNL, the problem of fabricating a gold film thin enough to allow for valid EELS measurements needed to be solved. One possible solution involved the use of gold nanoparticle solutions.

When particulate or colloidal solutions are applied to lacey TEM grids, the tendency is for the particles to adhere to the edges of the film as shown in Figure 9. The proposed method of creating a thin enough gold "film" was to apply gold nanoparticle solutions to the TEM grids in hope of creating aggregates of the gold particles that extend beyond the boundary of the lacey grid. This would, in effect, create a film of gold that could then be used as the experimental surface.

Gold nanoparticles were purchased from Ted Pella Inc. in 2, 5, 10, and 20 nm colloidal solutions. There are two methods that can be used in applying the particles to the grids. One is that you can float a grid on a drop of the solution for an extended amount of time. This would likely result in a monolayer of particles adhered to the grid. This method, however, did not result in enough of the particles aggregating on the grid to perform meaningful experiments. The other method is to place a drop on the solution on top of the grid and either allow it evaporate or cover the grid and allow some of the particles to settle on the grid. Although not necessarily guaranteeing a monolayer or particles, and in some areas

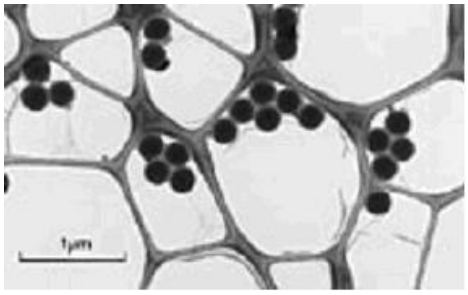

Figure 9: 0.26μm diameter Latex suspended on a Lacey Support Film (Image provided by www.tedpella.com)

resulted in particles present on both sides of the grid, this method did guarantee many more particles adhering to the grid. The images show in Figures 10 and 11, taken at SNL with Dr. Headley, show examples of 20 nm particles that have been evaporated onto the lacey Formvar grid.

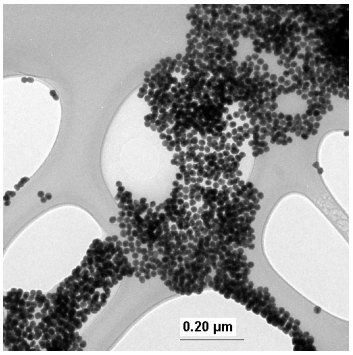

Figure 10: 20 nm evaporated gold particles

Clearly a single continuous monolayer is not present, but there are some areas in which the particles did form a small monolayer that spanned part of the opening on the lacey grid as highlighted in Figure 10, again taken at SNL. The ultimate goal of this procedure is to treat the nanoparticle layer as a semi-continuous gold film and adhere particular biology to the particles for experimentation. The immobilization chemistry involving the biology and the gold will be discussed in a subsequent section.

The gold nanoparticles are negatively charged, which allows them to stay suspended in water. Consequently, if one adds a positively charged ion to the solution, i.e. NaCl, the particles will tend to aggregate irreversibly as shown by Mirkin et al. [13]. It was thought

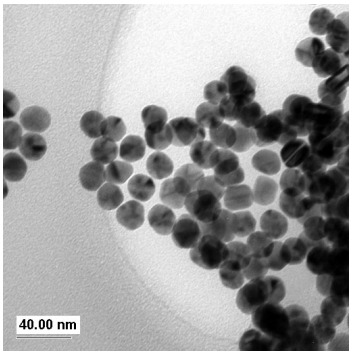

Figure 11: 20 nm evaporated gold particles magnified

that we could simply force the particles to aggregate then use the resulting clusters as the experimental surfaces. The results of adding a salt to the 5nm colloidal solution is shown in Figure 12. The resulting clusters were three-dimensional in fashion and contained several areas of multiple layers of particles, thus rendering much of the aggregate useless for our needs.

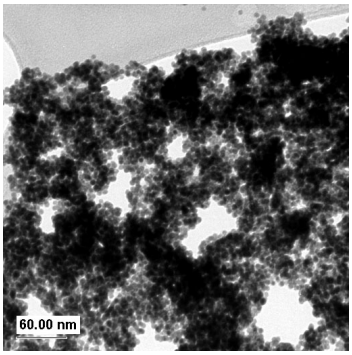

Figure 12: 5 nm particle aggregates

Another possibility was brought to our attention by Dr. Andrew Boal who is a post-doctoral researcher at SNL. He gave to me some silicon nitride membrane window grids he purchased from SPI Supplies. The support grid consists of a silicon substrate with a 50 nm layer of Si_3N_4 deposited on top. The silicon substrate is then etched away to the Si_3N_4 layer leaving a perfectly transparent "window" of Si_3N_4 (Figure 13). This was intriguing because, as mentioned previously, Si_3N_4 was suggested by Dr. Wang here at Georgia Tech as a possible mechanical stability layer in the proposed device. With a stabilizing layer

of Si_3N_4, the electrons in the eventual device would have to penetrate through that layer anyway, so we thought it would be beneficial to investigate the use of these grids.

Figure 13: SEM image of a 100 nm Si_3N_4 membrane window grid (Image provided by www.2spi.com)

Dr. Boal suggested we use gold nanoparticles as the examination surface on the Si_3N_4. He proposed a procedure that would result in a potentially continuous monolayer of particles on the surface of the membrane. The procedure began applying self-assembling thiol or amine groups to the Si_3N_4 membrane. With a continuous layer of thiol groups adhered to the membrane, gold nanoparticles inherently have an affinity for those groups and will bind to the groups in a single layer (Figure 14).

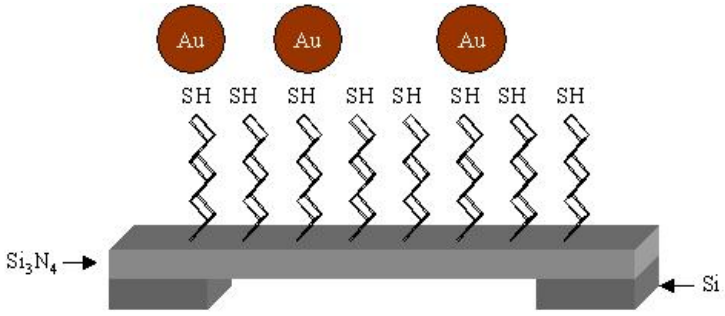

Figure 14: Diagram of Au particle monolayer on thiol groups

There are a couple of potential drawbacks in using the gold nanoparticle samples. One is the fact that the particles are, more or less, spherical in geometry. The spherical nature of the particles allows for multiple surface modes and coupling between particles, which could affect the resulting EELS spectra. Also, due to the fact that the gold nanoparticle "film" is porous, as clearly evident in Figure 10, biological specimens could potentially immobilize in between particles. This configuration, along with the interparticle coupling, could result in an EELS spectra drastically different than if a continuous gold film was used with the biology immobilized on only one side of the film (a configuration which is consistent with the traditional optically excited SPR sensors).

2.2.2 Fabrication and Application of Thin Gold Film Samples

Ted Pella Inc. offers a wide variety of TEM support grids for any kind of imaging process. This allowed for several different grids to be used in our EELS experimentation. As described above, one was the lacey Formvar coated grid. This grid is a copper grid covered with a holey film of Formvar and finally stabilized with carbon. The advantage of using a holey film covered grid is that although the holes in the copper grid themselves are small, they are extremely large in comparison to the size of typical electron microscopy specimens. The lacey film allows for viewing (and consequently EELS experiments) these small samples without the effects of an underlying support material. This was eventually found to be essential in our EELS investigations.

Although the nanoparticle approach to creating a gold film will be examined in the TEM, it was thought to be of great value to see if a truly continuous gold film could be fabricated and applied to the TEM grids. Mr. Ron Goeke in the thin films department at SNL provided me with one particular solution, which was eventually implemented and showed to work wonderfully.

It was suggested by Mr. Goeke that a layer of molybdenum be evaporated onto a silicon substrate. A 15nm gold layer was then evaporated on top of the molybdenum. The entire wafer would then be diamond cut into several small sections and each piece would be immersed in a 30% hydrogen peroxide solution. The peroxide dissolved the molybdenum layer

resulting in the 15nm gold film floating to the top of the solution in extremely small pieces. A TEM grid was then immersed in the peroxide and pulled out of the solution through the gold pieces floating on the surface. The result was a TEM grid with several regions covered with a 15nm gold film (Figure 15). This thin film was then used as the main experimental surface on which many of the experiments were carried out.

With the addition of the thin gold film as an experimental surface, a gold grid could also be useful. Luckily, Ted Pella also makes purely gold grids with no lacey films or stabilizing layers. When the thin gold film was adhered to the gold grid, the result was a TEM specimen holder made of pure gold, without the presence of any other material that could possibly interfere with the experiments. Although not as important in EELS, the use of the gold grid was particularly noticeable when taking energy dispersive spectroscopy (EDS) measurements.

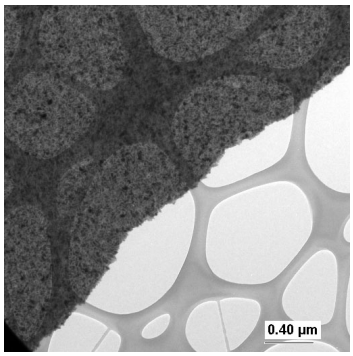

Figure 15: 15nm gold film on lacey TEM grid

2.2.3 Biology Used in Experimentation and Immobilization Protocols

Since the overall goal of this research is to develop a biosensor capable of detecting biological binding events, various biological specimens were to be used in the experimentation including DNA, protein A, and Bovine Serum Albumin (BSA). These were to be applied to the gold samples and the resulting EELS spectra were to be taken. Custom 12-base DNA was purchased from Alpha DNA and the strands were thiol modified for immobilization onto gold surfaces.

The immobilization schemes used were particularly simple because of the natural affinities for each of the chosen specimens to gold. This is precisely why these three molecules were chosen, so that the amount of chemistry needed for immobilization is minimized. For the protein A and BSA, the molecules were dissolved in PBS buffer and the TEM grids were submerged in the solution for anywhere from 30 minutes to overnight. The grids were then rinsed with deionized water and left to air dry.

The DNA immobilization was a little more complex. The strands used were as follows:

(1) 5'ATG CTC AAC TCT

(2) 5'AGA GTT GAG CAT

and strand (1) was modified with a chemically attached thiol group that has the form of

DNA-CH_2-CH_2-CH_2-CH_2-CH_2-CH_2-SH

and it is this SH end that will allow for bonding to a gold surface. The immobilization protocol for the DNA is shown below:

1. Dissolve each strand into 1mL 1xPBS.
2. Make stock solutions of each strand with a concentration of 1mg/mL.
3. Use this to make a stock solution of 10μg/mL.
4. Combine 250μL of each strand in a small vile and heat to 95°C for 5 minutes.
5. Lower temperature to 65°C for 20 minutes.
6. Cool at room temperature.

The DNA strands are now hybridized into groups of double stranded DNA. In order to adhere these strands to a gold surface, simply immerse the surface in a drop of the solution overnight in an airtight container. The sulfur at the end of the strands has an affinity for gold and the DNA self assembles on the gold.

2.2.4 Description of Electron Energy Loss Spectrum Collection Process

In TEM, a common material analysis technique is electron energy loss spectroscopy, or EELS. When an electron beam is incident onto a specimen, some of the electrons are inelastically scattered and lose energy. This energy loss is determined by the material through which the electron passes. In some cases the electron passes through the material unperturbed which are characterized by the zero-loss peaks on the EELS spectrum (Figure 16). Plasmon oscillations typically have energies of 10-40eV which will result in a peak on the EELS spectrum in that energy range (Figure 16). Multiple scattering events in the material give rise to additional peaks in the spectrum. Inelastic scattering of inner-shell electrons cause ionization peaks at significantly higher energy levels than those of the plasmons (Figure 17).

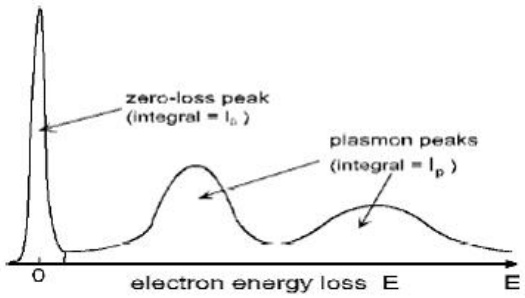

Figure 16: Low-loss region of EELS spectrum (Image provided in [15])

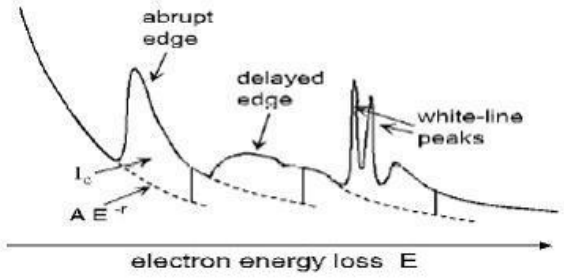

Figure 17: Inner shell-loss region of EELS spectrum (Image provided in [15])

In all of the experimentation done for this research, analysis of EELS spectra similar to those in the figures above was performed . Since the plasmon excitations are the only

physical phenomena of interest, we will only be interested in the low-loss region of the spectrum (Figure 16). After collecting the spectra in the TEM, the numerical data was stored in a data file which could then be imported to various analysis programs such as MS Excel or MATLAB. The data taken from several experimental samples was then processed and the results will be presented in Chapter 3.

CHAPTER III

RESULTS

In order to properly investigate the effects of binding events on the EELS spectrum of gold, several experimental runs must be performed. The following chapter presents the results of these experiments. It will also be shown mathematically in a later chapter where and why various problems in the spectra and the experimental process arose. For each of the spectra, the acceleration voltage of the TEM was 300kV and the angle of incidence was 0° with respect to the surface normal.

3.1 EELS of Gold Samples

To deduce any useful information from captured EELS spectra, we must first obtain a spectrum from a pure gold sample for comparison. EELS spectra from nearly all of the elements and certain compounds of elements can be found in several sources such as the Gatan EELS Atlas [16]. The best spectrum to which any of the later results would be compared would be one from a continuous slab of gold. Although readily found in the source mentioned above, we must capture this spectrum using the spectrometer in order to generate an accurate data file for further analysis. The spectrum captured is shown in Figure 18.

The plot shown in Figure 18 shows the electron energy loss spectrum of a thin gold film. The x-axis has units of electron-volts (eV) and represents how many eV an electron loses as it traverses the thickness of the film. The y-axis simply counts the number of electrons that lose a particular amount of energy. In the raw data for an EELS spectrum, the y-axis varies from 0 to several millions of electrons. Since this spectrum will be the one to which all subsequent spectra are compared, the y-axis was normalized in this and all spectra to follow. Since we are interested only in the plasmon region, or low-loss region, of the spectra, we will magnify a particular portion of the spectra herein. The magnified portion of interest

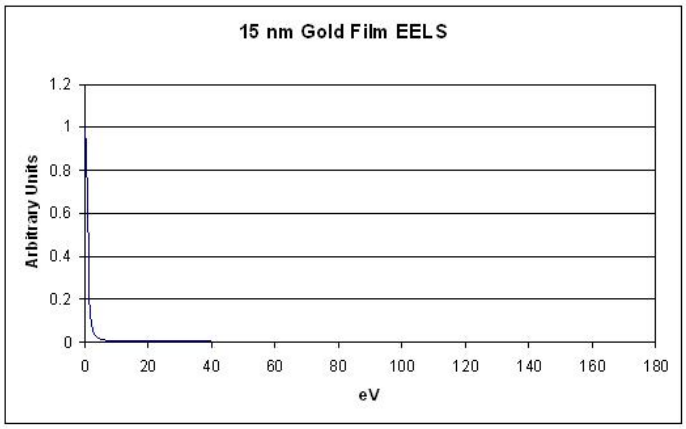

Figure 18: EELS spectrum from 15nm gold film

in the gold spectrum is shown in Figure 19.

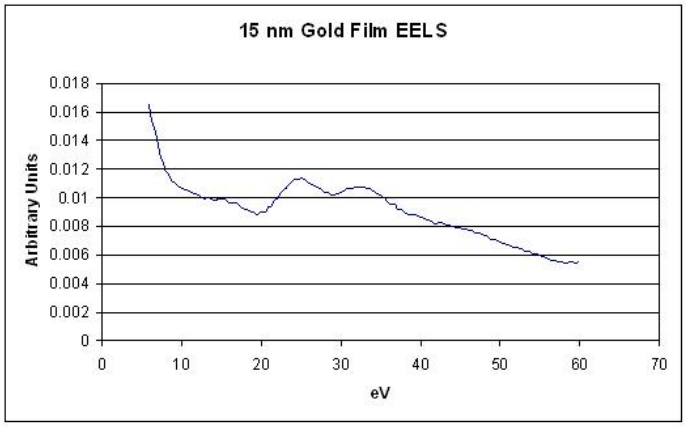

Figure 19: Low-loss region of the EELS spectrum from 15nm gold film

Figure 19 shows the plasmon region of the gold EELS spectrum. Important points to notice on this spectrum are the two peaks at approximately 25 and 33eV. The goal of this research is to investigate the changes in those peaks with the addition of various biology on the surface of the gold, whether it be peak broadening, peak shifting, or multiple plasmon peaks. When the sample gets too thick, sometimes extra peaks can arise at integer multiples of the plasmon energy loss because scattered electrons inside the medium can excite more than one plasmon. Peak shifting would be the most interesting consequence because

it would mean that the binding event changed the actual dielectric properties of the gold and would affect the response of the gold film to the electron beam.

3.1.1 EELS of Plain Gold Films

In order to ensure consistency in the experimental process, three spectra were taken from the pure gold film and are shown simultaneously in Figure 20. As clearly seen, each of the trials reveals nearly identical spectra, so any one of these spectra will be a suitable standard for comparison.

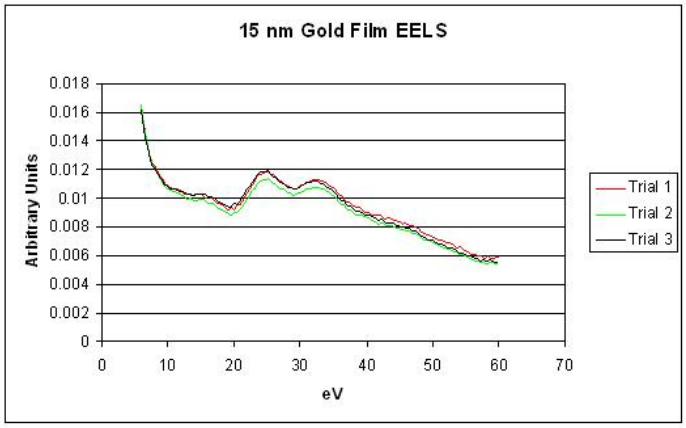

Figure 20: Spectra from three 15nm gold samples

Another useful technique for comparing various spectra is looking at the derivatives of the spectra themselves. It will be seen later that if there are, in fact, peak shifts in the spectra it is much easier to determine the actual shift when looking at the zero crossings of the derivatives rather than trying to estimate it from the real captured plots. The derivative will be simply calculated using the difference equation

$$y(n) = x(n+1) - x(n) \tag{11}$$

where $y(n)$ is the derivative and $x(n+1)$ and $x(n)$ are simply the collected data points. The derivatives of the three gold spectra are shown in Figure 21.

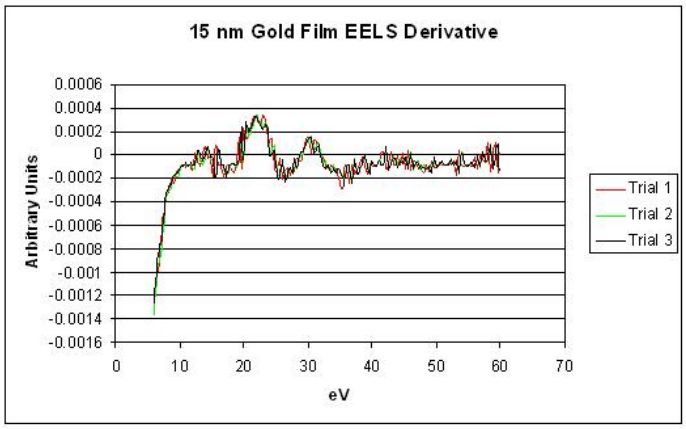

Figure 21: Derviatives of spectra from three 15nm gold samples

Looking at the derivatives of the spectra, it is still quite difficult to obtain any useful information due to the noise on the plots. This is simply because the EELS collection process contains unavoidable noise and results in an EELS spectrum that is not necessarily smooth. To eliminate the high frequency components of the plots, the following averaging filter will be used herein in order to clarify them.

$$y(n) = \frac{1}{3}\Big[x(n+1) + x(n) + x(n-1)\Big] \tag{12}$$

The result of the above operation is shown in Figure 22.

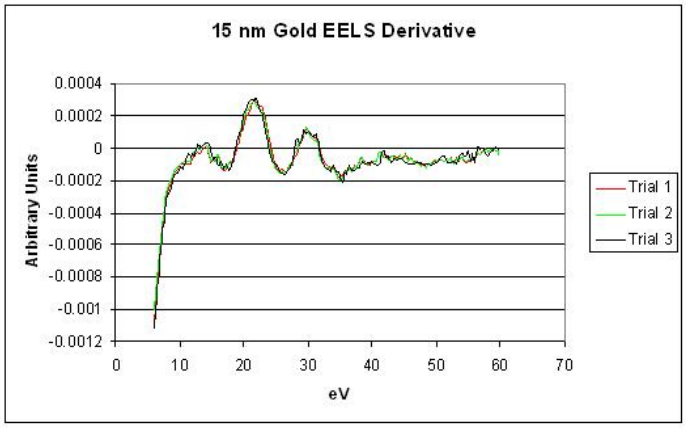

Figure 22: Derviatives of spectra from three 15nm gold samples

3.1.2 EELS of Gold Film with Biology

After the standard EELS spectra were taken from plain gold films, biology was added to the films to determine whether or not the spectra would change due to the binding event. Since BSA readily binds to gold, 1, 5, and 10mg/mL concentrations of BSA were applied to the gold in the manner described in the previous chapter. The results of these additions are shown in Figure 23 and the derivatives of the spectra are shown in Figure 24.

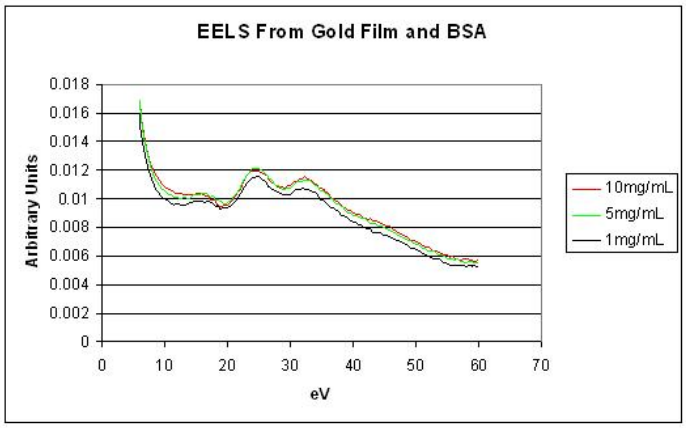

Figure 23: EELS from three 15nm gold films with varying BSA concentrations

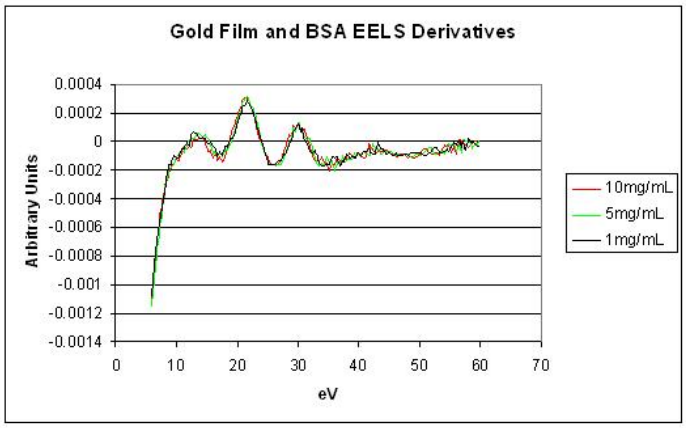

Figure 24: Derivatives of spectra from three 15nm gold films with varying BSA concentrations

Before one can make relevant conclusions from the above plots, one thing needs to be pointed out. After immobilizing the BSA, the effective sample becomes a two-layered

specimen: 15nm gold film, and a layer of BSA which is of finite average thickness. Bolton and Chen [14] have given a treatment of how to handle electron energy loss in multilayered slabs, the theory of which is beyond the scope of this thesis. However, it is shown that the peaks of the EELS spectra from a normally incident electron will be a result of coupled interface modes. In this case, there are three interfaces from two layers of material. The resulting EELS spectra will contain a combination of all of the excited modes at each interface.

Due to this multilayer effect, two questions now arise. One, is the contribution of the BSA so small that it can be considered negligible? And two, is the absence of any significant change in the spectra due to the fact that the biology is being destroyed inside the TEM due to the high vacuum and prolonged exposure to extremely high-energy electrons? The first question cannot be answered without an in-depth understanding of the dielectric function of the biology. This was not considered. A possible answer to the second question regarding the destruction of the biology was given at by Mirkin [13]. He pointed out that in solution TEM experiments, dehybridization of DNA takes place after prolonged irradiation from electron beams. This fact is precisely why DNA was not used in this experimentation. However, it may be able to be assumed that since Mirkin observed effective destruction of a biological molecule in the TEM, and since we are most likely using significantly higher electrons (300keV as opposed to 100keV), that the BSA may be getting destroyed almost instantaneously with the application of the electron beam. As will be shown in the following section, these two questions continued to puzzle us during the experimentation.

3.2 EELS of Silicon Nitride Samples

The method suggested by Dr. Boal using a monolayer of gold particles on a thin silicon nitride membrane was used. The procedure is as follows:

1. Clean grid in O_3 cleaner. This will clean and activate the surface for immobiliation.
2. In fume hood, cover grids in acetone for 1-2 minutes.
3. Add amine or thiol groups to acetone and let sit for another few minutes.
4. Rinse in clean acetone for 1-2 minutes.
5. Let air dry then float grid on a drop of gold particles for 15-20 minutes.

3.2.1 EELS of Functionalized Silicon Nitride Samples Without Biology

Floating the grid on a drop of particles, rather than letting a drop evaporate onto it, will result in a monolayer of particles instead of introducing the possibility of particles stacking on top of each other. However, like in the section above, we first had to take a reference spectrum from plain Si_3N_4 which is shown in Figure 25 and its derivative is shown in Figure 26. Although the plasmon peaks have slightly different amplitudes (Figure 25), their locations are nearly identical (Figure 26). The locations of these peaks are all we are concerned with.

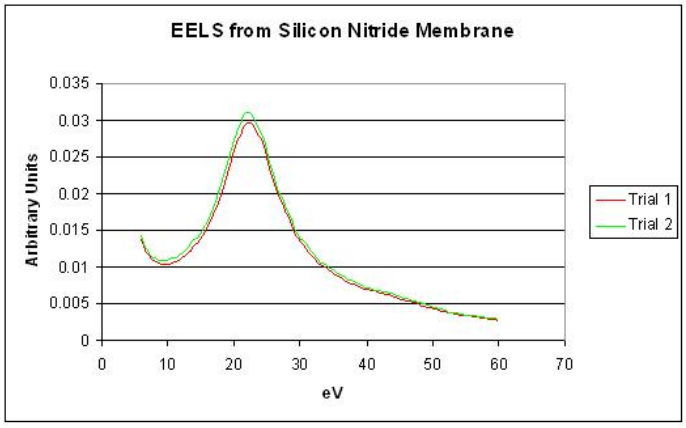

Figure 25: Spectra of Si_3N_4

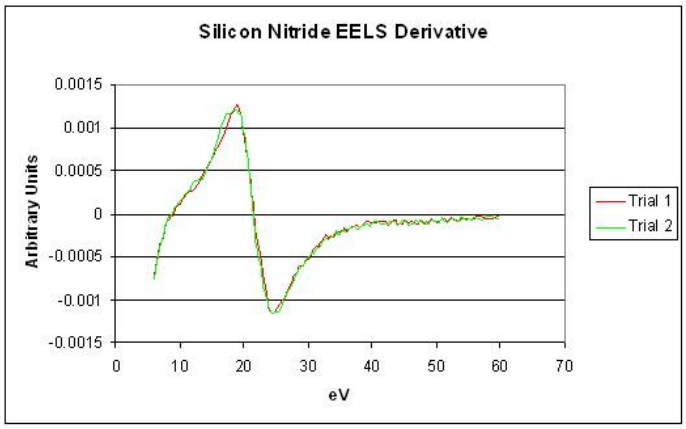

Figure 26: Derivatives of Si_3N_4 spectra

Since the gold nanoparticles are to be adhered to an amine layer which is immobilized on the Si_3N_4 membrane, the spectrum due to the added amine layer must also be taken, the results of which are shown in Figures 27 and 28.

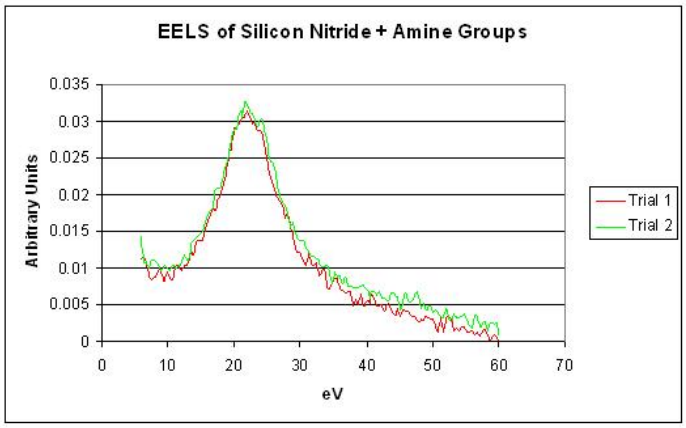

Figure 27: Spectra of Si_3N_4 plus an amine layer

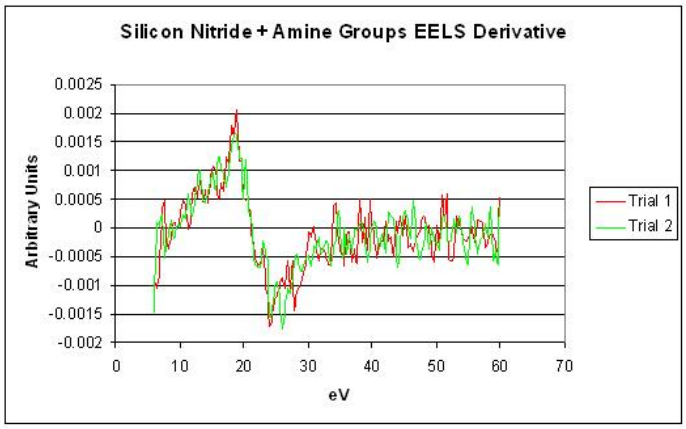

Figure 28: Derivatives of Si_3N_4 plus amine spectra

For the Si_3N_4 grids, 10nm gold nanoparticles were used. These particles were immobilized to the membrane surface by way of the added amine layer. The EELS due to the addition of these added particles is shown in Figures 29 and 30.

As said before, the goal of these experiments is to analyze the shifts of the plasmon peaks, if any, due to various binding events. In the case described in this section thus far, the addition of the amine groups and the gold particles will be compared to the original Si_3N_4 spectra. For the comparison, only the respective derivatives will be shown (Figure 31). Clearly we cannot deduce much from the plots in Figure 29. A magnified plot highlighting the zero crossings of the derivatives is shown in Figure 32. As seen in the plot, the shifts are only on the order of 1eV or so. The energy resolution of the spectrometer used in the experimentation is about 1-2eV. Therefore, the energy shifts shown in Figure 32 are below, or on the order of, the resolution of the system. Consequently, no significant conclusion could be made.

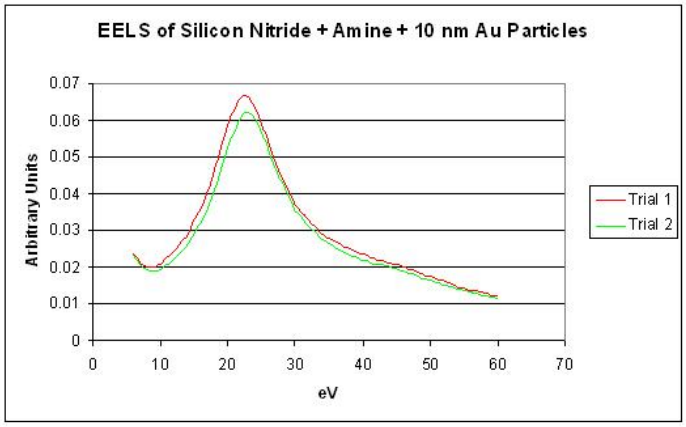

Figure 29: Spectra of Si_3N_4 plus an amine layer and 10nm gold particles

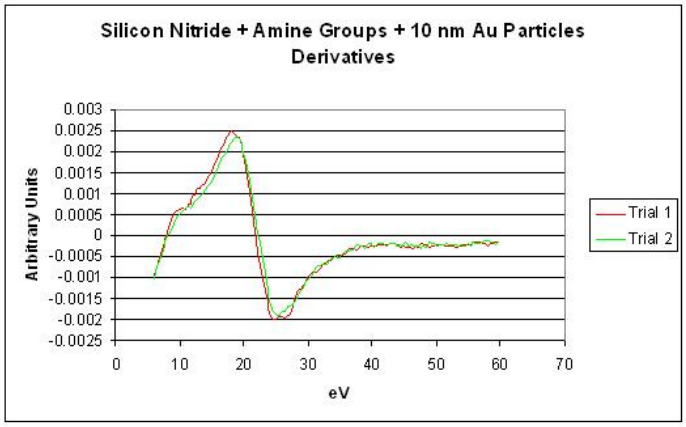

Figure 30: Derivatives of Si_3N_4 plus amine spectra

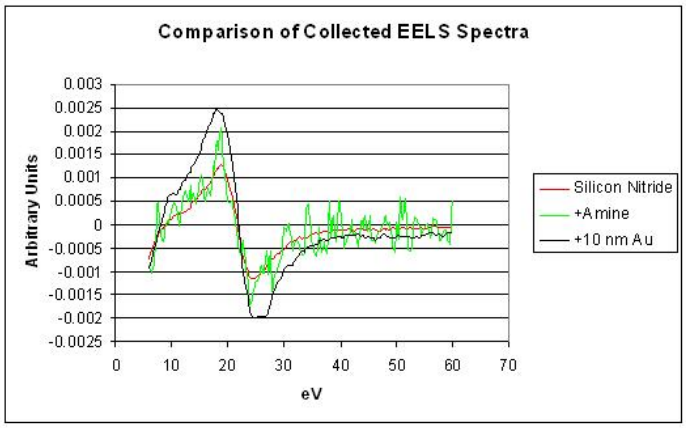

Figure 31: Derivatives of collected spectra

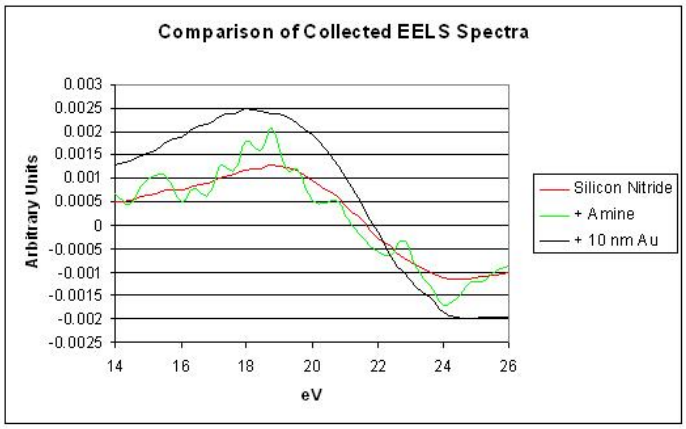

Figure 32: Magnified derivatives of collected spectra

3.2.2 EELS From Silicon Nitride Samples With the Addition of Biology

As before with the pure gold films, BSA was applied to the functionalized Si_3N_4 which contained the amine groups and the gold nanoparticles. In this case, the two extreme concentration, 1 and 10mg/mL, were used. The results are shown in Figure 33 and the derivatives of the spectra are shown in Figure 34.

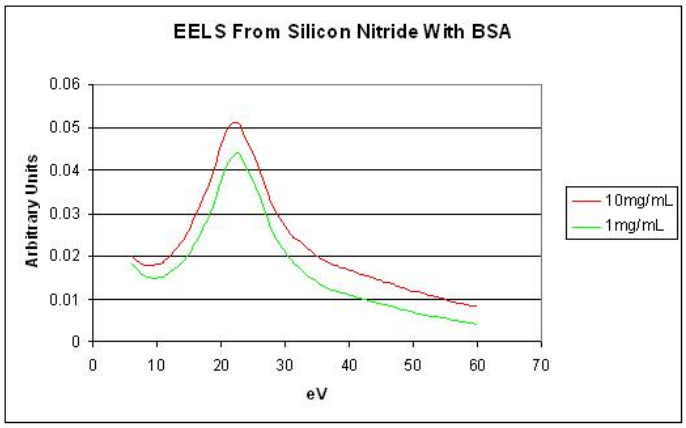

Figure 33: EELS spectra of Si_3N_4 with BSA

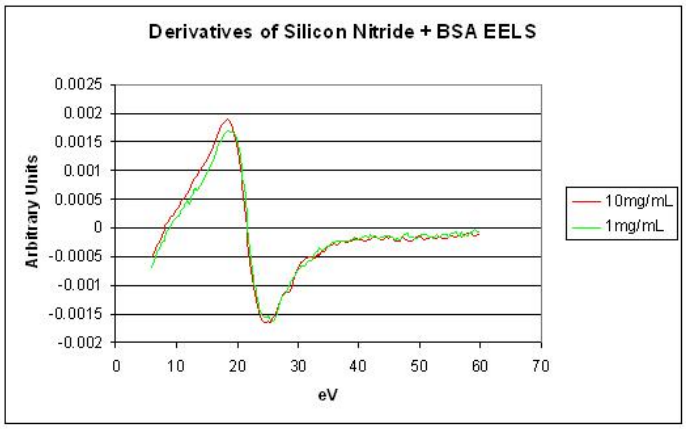

Figure 34: Derivatives of Si_3N_4 with BSA spectra

As noticed, the peak of the higher concentration plot is greater than that of the lower concentration. This could simply be because each of the data sets were normalized to the zero-loss peak, the magnitude of which is not necessarily consistent between successive spectrum captures. Nonetheless, it is clear that the location of the peaks did not change at all with respect to the original Si_3N_4 data. This data, like that from the gold film samples in the previous section, is therefore inconclusive.

As it was shown, the addition of biology to gold specimens with known EELS spectra showed no deviations from the reference spectra in terms of peak shifts, if any deviations at all. Chapter 4 will discuss the more intricate physics involved with these processes and formally introduce the concept of the loss function and the definition of the surface excitation probability. After these concepts are introduced mathematically, they will be used to determine whether or not it is even possible to deduce any information due to surface plasmon oscillations using our experimental setup.

CHAPTER IV

ANALYSIS OF RESULTS AND CONCLUSIONS

As shown in the previous chapter, the results of the experimentation were inconclusive and caused several questions to be raised. Was there something wrong with our procedure? Are the effects from surface plasmons for our purposes just too small to be measured? This chapter will discuss electron energy loss theory as well as attempt to answer those questions above.

4.1 Origination of Excitation Probability

In 1952, Pines and Bohm [3] suggested that some of the energy losses experienced by fast electrons passing through foils are due to the excitation of plasma oscillations or "plasmons" in the sea of conduction electrons. A summary of this treatment is given by Ritchie [5] and also by Aizpurua [17] and will be described below with any omitted steps in the cited papers included for completeness.

Assuming that the material of interest is described by a dielectric function $\varepsilon(\mathbf{k}, \omega)$ which depends both on the wave vector $\mathbf{k}$ and the wavelength of the disturbance, Poisson's equation must be satisfied:

$$\nabla^2 \phi(\mathbf{r}, t) = -\frac{\rho(\mathbf{r}, t)}{\varepsilon_0 \varepsilon_r(\mathbf{k}, \omega)}. \tag{13}$$

In frequency space,

$$\phi(\mathbf{k}, \omega) = -\frac{\rho(\mathbf{k}, \omega)}{k^2 \varepsilon_0 \varepsilon_r(\mathbf{k}, \omega)}, \tag{14}$$

where the four-dimensional Fourier transform has been employed on the potential and the charge distribution. For a fast electron of velocity $\mathbf{v}$, let us assume that the respective charge distribution is $\rho(\mathbf{r}, t) = -e\delta(\mathbf{r} - \mathbf{v}t)$ with e being the charge of an electron. The delta function in this case is a Kronecker delta giving a value of 1 when $\mathbf{r} = \mathbf{v}t$. The next step is to covert the delta function to frequency space using a four-dimensional Fourier

transform:

$$\rho(\mathbf{k},\omega) = \iint \delta(\mathbf{r}-\mathbf{v}t)e^{-i(\mathbf{k}\cdot\mathbf{r}+\omega t)}\,d\mathbf{r}\,dt. \tag{15}$$

When evaluating this integral at $\mathbf{r} = \mathbf{v}t$, the Fourier transform gets reduced to one-dimensional in t. The result is

$$\begin{aligned}\rho(\mathbf{k},\omega) &= \int e^{-i(\mathbf{k}\cdot\mathbf{v}+\omega)t}\,dt \\ &= \int e^{-i\mathbf{k}\cdot\mathbf{v}t}e^{-i\omega t}\,dt \\ &= 2\pi\delta(\mathbf{k}\cdot\mathbf{v}+\omega).\end{aligned} \tag{16}$$

The final form of the wave vector and frequency dependent potential is then given as

$$\phi(\mathbf{k},\omega) = -\frac{2\pi e\delta(\mathbf{k}\cdot\mathbf{v}+\omega)}{k^2\varepsilon_0\varepsilon_r(\mathbf{k},\omega)}, \tag{17}$$

with

$$\phi(\mathbf{r},t) = \frac{1}{(2\pi)^4}\iint \phi(\mathbf{k},\omega)e^{i(\mathbf{k}\cdot\mathbf{r}+\omega t)}\,d\mathbf{k}\,d\omega. \tag{18}$$

The total energy loss is related to the excitation probability by

$$\Delta W = \int_0^\infty d\omega\,\hbar\omega\frac{dP(\omega)}{d\omega}. \tag{19}$$

ΔW denotes the total energy loss of the incoming electron and if we are able to express the energy loss $d\Delta W/dx$ per unit path length as an integral over $\mathbf{k}$ and ω, the excitation probability is then known.

The energy loss per unit length in the medium is given by

$$-\frac{d\Delta W}{dx} = \frac{e}{v}\mathbf{v}\cdot\mathbf{E}, \tag{20}$$

evaluated at $\mathbf{r} = \mathbf{v}t$. Starting from our expression for the potential, a derivation of the interaction probability will be presented:

$$\phi(\mathbf{r},t) = -\frac{e}{(2\pi)^3\varepsilon_0 v}\int_{-\infty}^{\infty} d\mathbf{k}\int_{-\infty}^{\infty} d\omega\,e^{i(\mathbf{k}\cdot\mathbf{r}+\omega t)}\frac{\delta(\mathbf{k}\cdot\mathbf{v}+\omega)}{\varepsilon_r(\mathbf{k},\omega)k^2}. \tag{21}$$

Taking the gradient to find the electric field, we get

$$-\nabla\phi(\mathbf{r},t) = -\frac{ie}{(2\pi)^3\varepsilon_0 v}\int_{-\infty}^{\infty} d\mathbf{k}\int_{-\infty}^{\infty} d\omega\,e^{i(\mathbf{k}\cdot\mathbf{r}+\omega t)}\frac{\delta(\mathbf{k}\cdot\mathbf{v}+\omega)}{\varepsilon_r(\mathbf{k},\omega)k^2}\mathbf{k}. \tag{22}$$

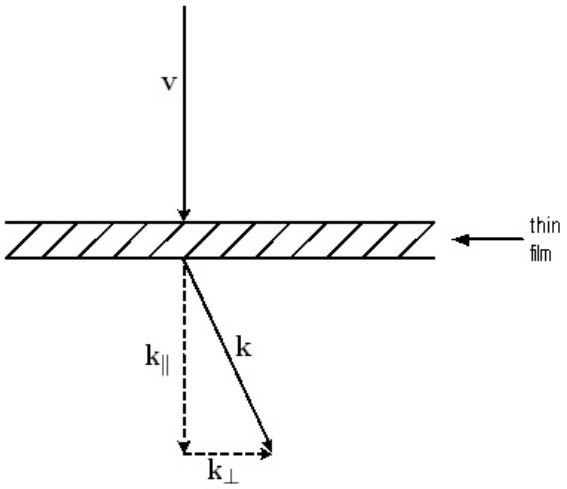

Figure 35: Schematic of momentum transfer

Now, the $\mathbf{k}$ vector will be divided into $\mathbf{k}_\perp$ and $\mathbf{k}_\parallel$ which are perpendicular and parallel to the velocity, respectively. This is roughly shown schematically in Figure 35.

The energy loss per unit path length as defined above is then given by:

$$\frac{d\Delta W}{dx} = \frac{ie}{(2\pi)^3\varepsilon_0 v}\int_{-\infty}^{\infty} d\mathbf{k}_\perp \int_{-\infty}^{\infty} d\mathbf{k}_\parallel \int_{-\infty}^{\infty} d\omega\, e^{i\mathbf{k}_\perp\cdot\mathbf{v}t}\, e^{i\mathbf{k}_\parallel\cdot\mathbf{v}t}\, e^{i\omega t}$$

$$\frac{\delta(\mathbf{k}_\perp\cdot\mathbf{v}+\mathbf{k}_\parallel\cdot\mathbf{v}+\omega)}{\varepsilon_r(\mathbf{k},\omega)k^2}(\mathbf{k}_\perp\cdot\mathbf{v}+\mathbf{k}_\parallel\cdot\mathbf{v}). \tag{23}$$

Since $\mathbf{k}_\perp$ is perpendicular, any $(\mathbf{k}_\perp\cdot\mathbf{v})$ terms go to zero. The product $(\mathbf{k}_\parallel\cdot\mathbf{v}) = \frac{\omega}{v}$ and the k^2 term then becomes $(k_\perp^2 + (\frac{\omega}{v})^2)$. Integrating over $\mathbf{k}_\parallel$ at the point inside the delta function where $-\mathbf{k}_\parallel\cdot\mathbf{v} = \omega$, we get:

$$\frac{d\Delta W}{dx} = \frac{ie^2\omega}{(2\pi)^2\varepsilon_0 v^2}\int_{-\infty}^{\infty} dk_\perp \int_{-\infty}^{\infty} d\omega\, \frac{1}{\varepsilon_r(\mathbf{k},\omega)(k_\perp^2+(\frac{\omega}{v})^2)}. \tag{24}$$

The ω integral can be simplified further using the properties of parity of the dielectric function ($\varepsilon(\mathbf{k},-\omega) = \varepsilon^*(\mathbf{k},\omega)$). For the next few steps, we will define $F(\omega) = \frac{1}{\varepsilon_r(\mathbf{k},\omega)(k_\perp^2+(\frac{\omega}{v})^2)}$.

$$\begin{aligned}
\int_{-\infty}^{\infty} F(\omega)\, d\omega &= \int_0^{\infty} F(\omega)\, d\omega + \int_{-\infty}^{0} F(\omega)\, d\omega \;\rightarrow\; (\omega' = -\omega) \\
&= \int_0^{\infty} F(\omega)\, d\omega - \int_{\omega'=-\infty}^{0} F(\omega')\, d\omega \;\rightarrow\; (\omega = \omega') \\
&= \int_0^{\infty} F(\omega)\, d\omega + \int_0^{\infty} F(-\omega)\, d\omega
\end{aligned}$$

$$
\begin{aligned}
&= \int_0^\infty \left(F(\omega) + F^*(\omega)\right) d\omega \\
&= \int_0^\infty 2\,\mathrm{Re}F(\omega)\, d\omega
\end{aligned} \tag{25}
$$

Plugging this result into Equation 20, the final equation we arrive at is

$$
\frac{d\Delta W}{dx} = \frac{e^2\omega}{2\pi^2\varepsilon_0 v^2}\int_{-\infty}^{\infty} dk_\perp \int_0^\infty d\omega\, \mathrm{Im}\Big(-\frac{1}{\varepsilon_r(\mathbf{k},\omega)}\Big)\frac{1}{(k_\perp^2 + (\frac{\omega}{v})^2)}. \tag{26}
$$

Now according to Equation 19,

$$
\frac{d^3P}{dx d\mathbf{k}_\perp d\omega} = \frac{e^2}{2\pi^2\hbar\varepsilon_0 v^2}\mathrm{Im}\Big(-\frac{1}{\varepsilon_r(\mathbf{k},\omega)}\Big)\frac{1}{(k_\perp^2 + (\frac{\omega}{v})^2)}, \tag{27}
$$

which is the excitation probability per unit frequency per unit path length per unit momentum transfer. $\mathrm{Im}(-\frac{1}{\varepsilon_r(\mathbf{k},\omega)})$ is known as the *loss function* of the particular material. The loss function is given by

$$
\mathrm{Im}\Big(-\frac{1}{\varepsilon_r(\mathbf{k},\omega)}\Big) = \frac{\varepsilon_i}{\varepsilon_r^2 + \varepsilon_i^2}. \tag{28}
$$

Using the form of the dielectric function in Equation 1 from Chapter 1, we find that

$$
\varepsilon_r(\omega) = 1 - \frac{\omega_p^2}{\omega^2 + 1/\tau^2} \quad \text{and} \quad \varepsilon_i(\omega) = \frac{\omega_p^2}{\omega\tau(\omega^2 + 1/\tau^2)}. \tag{29}
$$

Finally,

$$
\mathrm{Im}\Big(-\frac{1}{\varepsilon_r(\mathbf{k},\omega)}\Big) = \frac{\omega_p^2\omega/\tau}{(\omega^2 - \omega_p^2)^2 + \omega^2/\tau}. \tag{30}
$$

Analyzing Equation 30, one notices that the peak of the excitation probability for an electron in a bulk medium is given by the poles of the loss function. The locations of these poles are at the plasma frequency and correspond to an excitation of the electron gas at that frequency. However, this is only valid for an infinite bulk material. As mentioned in Chapter 1, Ritchie [5] went on to derive the excitation probability for an electron passing through a finite crystal. This was calculated by finding a nontrivial solution to Poisson's equation including realistic boundary conditions which Gabor [4] overlooked. The result of this calculation for a film of thickness d_0 after integrating over x and $\mathbf{k}_\perp$ is [7]

$$
\begin{aligned}
\frac{dP}{d\omega} = \frac{e^2}{2\pi^2\hbar\varepsilon_0 v^2}\int_0^{2\pi q_c} dk_\perp \Bigg\{ &\mathrm{Im}\Big(-\frac{1}{\varepsilon}\Big)\frac{d_0 k_\perp}{(k_\perp^2 + (\frac{\omega}{v})^2)} \\
&+ \frac{k_\perp^2}{(k_\perp^2 + (\frac{\omega}{v})^2)^2}\mathrm{Im}\Big[\frac{1-\varepsilon}{\varepsilon}\cdot\frac{2(\varepsilon-1)\cos(\omega d_0/v) + (\varepsilon-1)e^{(-k_\perp d_0)} + (1-\varepsilon^2)e^{(k_\perp d_0)}}{(\varepsilon-1)^2 e^{(-k_\perp d_0)} - (\varepsilon+1)^2 e^{(k_\perp d_0)}}\Big]\Bigg\},
\end{aligned}
$$

where q_c is known as the cutoff wave vector. As shown in Figure 35, an electron that passes through a film will experience momentum transfer $k_\perp$. It is required that we integrate over all momentum transfers up to the cutoff wave vector in order to assure the integral does not diverge when calculating the excitation probability per unit energy. Integrating over x simply integrates over the entire path length of the electron which is parallel to the original velocity vector. Hence, the first term is simply d_0 times the excitation probability of an infinite medium. The second term represents the boundary correction. This shows that the excitation probability is governed by both the bulk and the interface itself. The surface plasmon resonates at a frequency $\omega_p/\sqrt{2}$, as was shown in Chapter 1. An experimentally observed spectrum, therefore, is a superposition of the bulk and the surface energy losses. This demonstrates the first problem in our experimentation: EELS spectra contain a combination of both volume and surface excitations.

The equation for the excitation probability above which now includes the correction for the existence of the surface will now be examined assuming that the thickness of the metal is large enough such that the coupling between the surfaces can be ignored and the Im{} terms in the boundary correction reduce to [19]

$$\mathrm{Im}\left\{\frac{(\varepsilon-1)^2}{\varepsilon(\varepsilon+1)}\right\} = \mathrm{Im}\left\{\frac{1}{\varepsilon} - \frac{4}{\varepsilon+1}\right\} \tag{31}$$

As noted previously, the first term is the volume plasmon energy loss function. The second term is known as the surface plasmon energy loss function. In order to calculate these function, the dielectric function of gold is needed. The dielectric function can be calculated from the Handbook of Optical Constants of Solids edited by Palik [18]. However, what is tabulated in the book is the frequency-dependent complex index of refraction given by

$$n(\omega) = n_r(\omega) + in_i(\omega). \tag{32}$$

Since the dielectric function is simply given by n^2, the result is

$$\varepsilon(\omega) = \varepsilon_r(\omega) + i\varepsilon_i(\omega), \tag{33}$$

such that $\varepsilon_r = n_r^2 - n_i^2$ and $\varepsilon_i = 2n_r n_i$. The plot of the real and imaginary parts of the dielectric function are shown in Figure 36 and the corresponding bulk and surface loss

functions are shown in Figure 37.

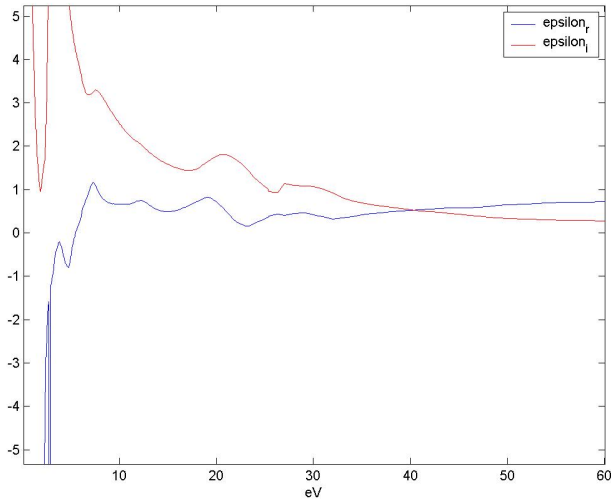

Figure 36: Dielectric function of gold

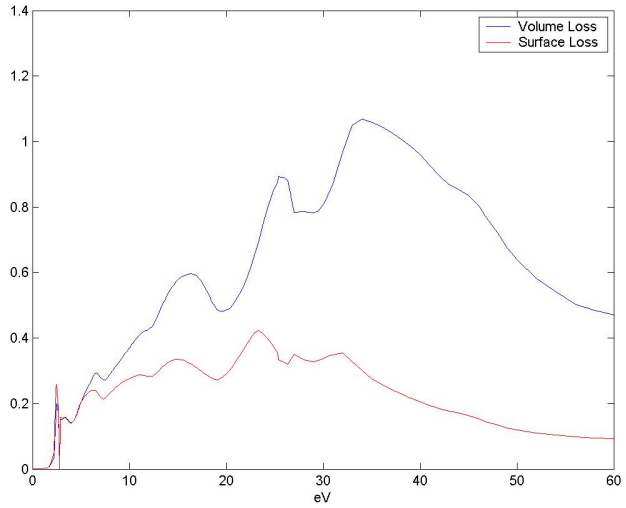

Figure 37: Volume and surface plasmon losses in gold

4.2 Analysis of the Excitation Probabilities

Dr. Wang here at Georgia Tech informed us of a way to isolate the contribution from surface excitations from the entire EELS spectrum. Let us define the total excitation probability in a thin film as P_1 and that of a bulk material as P_2. The portion of P_1 that is due to the surface excitations, which we will call P_s in the film is approximately given by

$$P_s \approx P_1 - \frac{d_1}{d_2} P_2, \tag{34}$$

where d_1 and d_2 are the thicknesses of the thin film and the bulk material, respectively. In the following calculations, $d_1 = 15\text{nm}$ which is the thickness of the film used in Chapter 3 and $d_2 = 300\text{nm}$. A FORTRAN program provided by Dr. Z.L. Wang is then used to calculate the excitation probabilities. The source code for this program is found in Appendix A. A cutoff wave vector of 1000nm^{-1} was used and the total excitation probability as well as the surface and bulk excitation probabilities were calculated for different incoming electron energies. Shown in Figure 38 is the total surface plasmon excitation probability versus increasing acceleration voltage (and hence velocity) of an incoming electron. It also includes how much of the overall spectrum of a 15nm film is due to that of the surface plasmons as given by Equation 34.

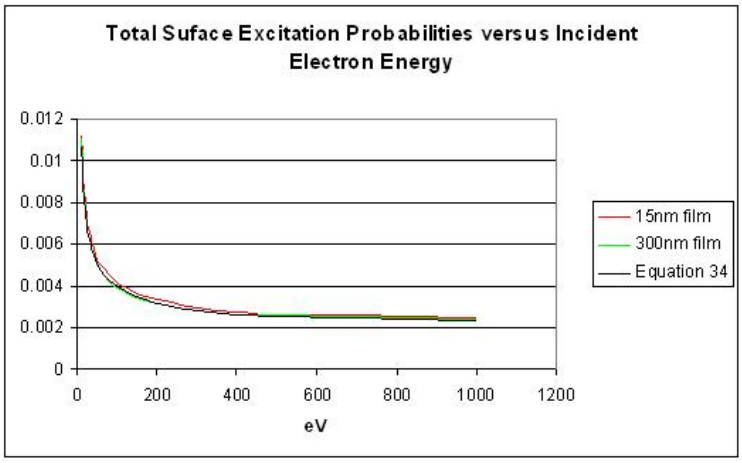

Figure 38: Total surface plasmon excitation probabilities

As clearly shown in Figure 38, the surface excitation probability for a thin film is nearly identical to that of the bulk. It is also clear that the total surface excitation probability in the 15nm film given by Equation 34 is nearly identical to that of the surface and the bulk components of the boundary corrected equation given by Wang [7]. Shown in Figure 39 is the total bulk plasmon excitation probability. Note that the bulk probability for a thick film is significantly greater than that of a thin film. This is because the electron spends more time inside a bulk material than it does in a thin film thus allowing for more bulk excitations.

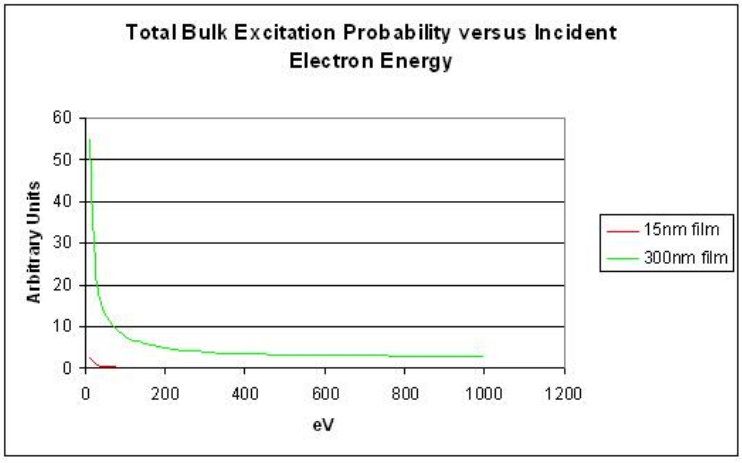

Figure 39: Total bulk plasmon excitation probabilities

An interesting consequence of the addition of the boundary correction in Ritchie's work is shown in Figure 40. This plot shows the ratio of the surface plasmon excitation to the bulk excitation. Note how the effect of the surface plasmon on the overall excitation probability increases both with increasing incident electron energy and decreasing film thickness. Both are consequences of the amount of time the electron spends traversing the material. Higher velocities along with thinner samples allow for less time for the electron to excite bulk excitations and as the sample gets thinner and thinner, the surface excitation will begin to appear more prominent in the overall excitation probability.

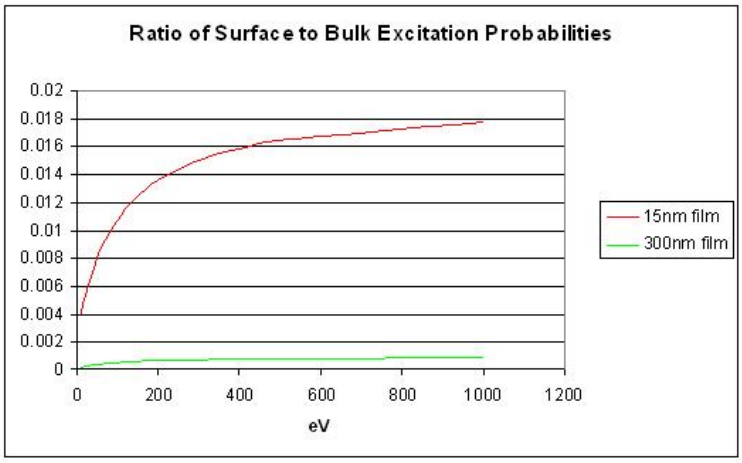

Figure 40: Ratio of surface to bulk excitation probabilities

4.3 Concluding Remarks

One simple conclusion regarding the velocity of the electrons that should be used in a potential sensing device (assuming a normally incident electron with respect to the 15nm gold film) is clearly deduced from Figure 41. As the incident energy of the electron increase, the overall excitation probability decreases significantly.

Figure 41 then, along with Figure 38, shows that a normally incident trajectory is obviously not the best choice for the incident electron. Garcia-Molina et al. [20], among others, have shown that an electron travelling parallel to the boundary outside of the the material will experience only surface effects. This is actually quite obvious from the previous section in that since the electron does not travel inside the material itself, it cannot cause bulk

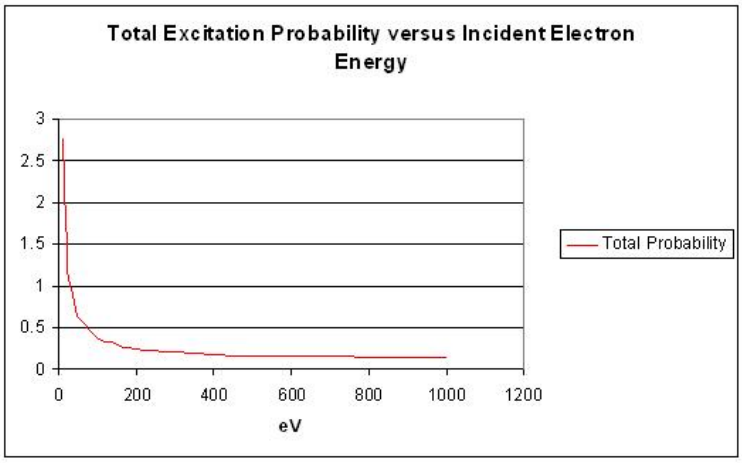

Figure 41: Total excitation probability in 15nm gold film

excitations. One can now reasonably assume that as the angle of incidence of the electron increases with respect to the surface normal, the EELS spectrum will show an increase in the effects of surface excitations as opposed to the bulk effects dominating, with the perpendicular and parallel trajectories obviously being the limiting cases. Oblique incidences have been treated by Otto [21], Kröger [22], and Geiger [23], however, the mathematics involved with the oblique incidences become quite involved and are beyond the scope of this thesis.

Another problem that can arise is the use of relativistic electrons. A 300keV electron has a velocity of about $0.78c$, with c being the speed of light. Traditional non-relativistic theory ignores retardation effects and when an electron passes by a dielectric medium, Cerenkov radiation can occur due to the relativistic effects as shown by Kröger [22]. Thus, EELS spectra will be affected by both plasmon excitations as well as Cerenkov radiation. Since the FORTRAN program used to calculate the excitation probabilities ignored retardation effects, the resulting calculations are somewhat misleading. However, we can consider these to be "best-case-scenario" calculations, as the actual calculations that include retardation effects will show that the EELS spectra may contain, depending on film thickness and electron velocity and trajectory, significant contributions due to Cerenkov radiation. These effects can actually be seen to occur at energies as low as 100keV [20] and are surely much

more significant at our 300keV experimental electron energy. To eliminate this possibility, it would be of great value to use much lower energy electrons. On the other hand, as Tougaard and Kraaer [24] pointed out, the entire theoretical model used above breaks down for electrons with incident energy below about 2keV.

Yet another problem with the possibility of fabricating any type of device is that of the measurement of the plasmons. To our knowledge, it is not known whether or not a surface plasmon generates a surface current which can be measured electronically. However, since the plasmons oscillate at incredibly high frequencies (in the case of TEM, much higher than even optical frequencies), there is essentially no chance of measuring any type of currents induced on the film if, in fact, there are any to be measured at all. This leads us to an even greater problem: the only way to measure the energy loss of electrons due to plasmon oscillations is by using an electron energy loss spectrometer. This spectrometer is quite large, even on a macroscopic scale, and contains many mechanical components. So, the goal of this research is not just to create a novel eSPR sensing device, but to also shrink the electron energy loss spectrometer to a microscopic scale. This will most certainly take several years to realize. When it is realized, however, we do believe that the possibilities of an eSPR device are spectacular and surely merit further research when the time comes.

APPENDIX A

EXCITATION PROBABILITY FORTRAN PROGRAM

The FORTRAN program listed below calculates the single-loss EELS spectra of a thin crystal slab in TEM. The calculation is based on Eq. (8.3.37) with consideration of the excitation of the top and bottom surfaces of the foil. The slab thickness is d and the slab normal direction is the direction of the incident electron beam. The surface plasmon (SP) and volume plasmon (VP) excitations are distinguished according to the loss functions $\mathrm{Im}[-\frac{2}{\varepsilon+1}]$ and $\mathrm{Im}[-\frac{1}{\varepsilon}]$, respectively. The format of the input dielectric data is given. The output gives the EELS spectrum at 1eV/channel, surface and volume plasmon excitation probabilities, and the integrated total excitation probability P.

```
C TEELS.FOR
C
C by Z.L. Wang
C
C THIS PROGRAM CALCULATES THE VALENCE-LOSS (INCLUDING
C SURFACE AND VOLUME PLASMONS) SPECTRUM FOR A PARALLEL-
C SIDED SLAB USING RITCHIE'S NON-RELATIVISTIC THEORY.
C
C
INTEGER I,J,K
DIMENSION ER(50),EI(50),SPECSHP(50)
COMPLEX EE,QSA,UPPART,LOWPART
OPEN(UNIT=8, FILE='DIELEC.DAT', STATUS='OLD')
OPEN(UNIT=9, FILE='EXCPROB.DAT', STATUS='NEW')
OPEN(UNIT=11, FILE='SPECTRA.DAT', STATUS='NEW')
C INPUT ELECTRON VELOCITY V/C
```

```
5 WRITE(6,10)
10 FORMAT(2X,'Input electron velocity v/c ratio ...')
READ(5,*) V
IF(V.GE.1.0) GOTO 5
VL=1.0
VB=(V/VL)**2
WRITE(9,22) V
22 FORMAT(2X,'Electron velocity v/c = ',F10.8)
WRITE(11,22) V
C INPUT SPECIMEN THICKNESS
WRITE(6,30)
30 FORMAT(2X,'Input specimen thickness (in Angstrom)...')
READ(5,*) T
T=ABS(T)
WRITE(9,32) T
32 FORMAT(2X,'Specimen thickness d = ',F10.2,' Angstrom')
WRITE(11,32) T
C INPUT CUT-OFF WAVE VECTOR
WRITE(6,40)
40 FORMAT(2X,'Input cut-off wave vector (in 1/Angstrom)...')
READ(5,*) QC
WRITE(9,44) QC
44 FORMAT(2X,'Cut-off wave vector qc = ',F10.5,' 1/Angstrom')
WRITE(11,44) QC
QC=2.0*3.14159*ABS(QC)
C INPUT DIELECTRIC FUNCTION
C The dielectric function is given in file 8 of name
C DIELEC.DAT with an energy resolution of 1 eV (= 1 channel)
READ(8,45) NDP
```

```
45 FORMAT(2X,I2)
DO 50 I = 1, NDP
50 READ(8,60) ER(I), EI(I)
60 FORMAT(2X,F10.7,2X,F10.7)
C C HEADING FOR OUTPUT
WRITE(9,64)
64 FORMAT(2X,'EXCITATION PROBABILITIES:')
WRITE(11,66)
66 FORMAT(2X, 'ENERGY-LOSS EXC. PROB./eV')
SP=0.0
VP=0.0
C INTEGRATE OVER ENERGY-LOSS W
C DW is the energy resolution, DW = 1 means 1eV/channel.
DW=1.0
DO 400 J = 1, NDP
W=J
WW=W**2
C COMPLEX DIELECTRIC FUNCTION
EE=CMPLX(ER(J), EI(J))
C
QSA=CMPLX(0.0, 0.0)
C INTEGRATE OVER QY
NMAX1=4000
NMAX2=3000
NMAX=NMAX1+NMAX2
QYH=0.01
DO 600 K=1,NMAX
IF(K.GT.NMAX1) GOTO 80
QY=(K-1)*QYH/NMAX1+QYH/2.0
```

```
DQY=QYH/NMAX1
GOTO 85
80 QY=QYH+(K-NMAX1)*(QC-QYH)/NMAX2+QYH/2.0
DQY=(QC-QYH)/NMAX2
85 ALP=(QY**2+WW/(1969.0*V)**2)
QPP=QY**2/ALP**2
QYY=QY*T
IF(QYY.GT.50) QYY=50.0
UPPART=-DQY*QPP*((1.0-EE)/EE)*(2.0*(EE-1.0)*COS(W*T/(1973.2*V))
A +((EE-1.0)**2)*EXP(-QYY)+(1.0-EE**2)*EXP(QYY))
LOWPART=((EE-1.0)**2*EXP(-QYY)-(EE+1.0)**2*EXP(QYY))
QSA=QSA+UPPART/LOWPART
600 CONTINUE
C SURFACE PLASMON COMPONENT
SP=AIMAG(QSA)+SP
C VOLUME PLASMON COMPONENT
VP1=ALOG(1.0+(QC*V*1973.2/W)**2)*AIMAG(-1.0/EE)
VP=VP1+VP
C VALENCE-LOSS SPECTRUM
SPECSHP(J)=AIMAG(QSA)+T*VP1/2.0
400 CONTINUE
CONS=2.35E-6
C SURFACE PLASMON EXCITATION PROBABILITY
SP=SP*DW*CONS/V**2
C VOLUME PLASMON EXCITATION PROBABILITY
VP=VP*T*CONS*DW/V**2
VP=VP/2.0
C OUTPUT SINGLE-LOSS SPECTRUM
DO 350 J=1, NDP
```

```
SPECSHP(J)=SPECSHP(J)*CONS/V**2
WRITE(11,355)J, SPECSHP(J)
355 FORMAT(3X,'W=',I2,4X,'dP/dw =',F20.12)
350 CONTINUE
C TOTAL EXCITATION PROBABILITY
TS=VP+SP
ALAMEDA=T/VP
C OUTPUT SURFACE AND VOLUME PLASMON AND TOTAL EXCITATION C
PROBABILITIES
WRITE(9,700) SP,VP,TS
700 FORMAT(2X,'SP P =',F15.10,X,'VP P =',F15.10,X,
A 'TOTAL P =',F15.10)
WRITE(9,710) ALAMEDA
710 FORMAT(8X,'Inelastic mean-free-path =',F12.5,' Angstrom')
STOP
END
```

Input data file: DIELEC.DAT

Real and imaginary components of the dielectric function for Au. The dielectric function e is assumed to be independent of q. The first line is the number of channels. The data are inputted in a format of FORMAT(2X,F10.7,2X,F10.7) at 1 eV/Channel.

```
    50
-76.774500  6.52488000
-9.8949400  1.04600000
-1.1572700  6.40600000
-0.3221600  7.01200000
-0.4742400  4.85700000
0.31644800  3.71400000
1.10510000  3.21000000
```

0.87483600 3.21300000

0.69253100 2.87000000

0.66423100 2.52670000

0.65790000 2.26440000

0.74376000 2.06940000

0.64909100 1.86800000

0.53755100 1.71290000

0.49014400 1.58660000

0.54044100 1.48180000

0.60966400 1.43000000

0.72134400 1.47970000

0.82992500 1.64010000

0.72041600 1.76480000

0.48832500 1.80110000

0.25112100 1.67060000

0.15660000 1.50975000

0.25657500 1.19540000

0.35571600 1.01520000

0.34177500 1.21676800

0.39780000 1.13665000

0.44335200 1.09381400

0.46022400 1.08419000

0.42316000 1.06972200

0.36898500 1.01439200

0.32312500 0.91770000

0.34473600 0.80443000

0.38311200 0.73693400

0.42036800 0.68747400

0.44640000 0.65080800

0.46806300 0.61621600

0.48804000 0.58692200

0.50424000 0.55985800

0.52046900 0.53106000

0.53791200 0.50656600

0.55460700 0.48722400

0.56598500 0.47128800

0.57172500 0.45514800

0.57512500 0.43470000

0.58350900 0.40894000

0.59783700 0.38508400

0.61197100 0.36630000

0.62867200 0.34974600

0.64396800 0.33782400

REFERENCES

[1] Pirio, G., Legagneux, P., Pribat, D., Teo, K. B. K., Chhowalla, M., Amaratunga, G. A. J. and Milne, W. I., "Fabrication and Electrical Characteristics of Carbon Nanotube Field Emission Microcathodes With an Integrated Gate Electrode," *Nanotechnology*, Vol. 13, pp. 1-4, Oct. 2002

[2] Burstien, E., Chen, W. P., Chen, Y. J., and Hartstein, A., "Surface Polaritons - Propagating Electromagnetic Modes at Interfaces," *The Journal of Vacuum Science and Technology*, Vol. 11, No. 6, pp. 1004-1019, Nov./Dec. (1974)

[3] Pines, D. and Bohm, D., "A Collective Description of Electron Interactions: II. Collective vs. Individual Particle Aspects of the Interactions," *Physical Review*, Vol. 85, No. 2, pp. 338-353, Jan. 1952

[4] D. Gabor, Phil. Mag. **1**, 1 (1956)

[5] Ritchie, R. H., "Plasma Losses by Fast Electrons in Thin Films," *Physical Review*, Vol. 106, No. 5, pp. 874-881, June 1957

[6] Stern, E. A. and Ferrell, R. A., "Surface Plasma Oscillations of a Degenerate Electron Gas," *Physical Review* Vol. 120, No. 1, pp. 130-136, Oct. 1960

[7] Wang, Z. L., "Valence Electron Excitations and Plasmon Oscillations in Thin Films, Surfaces, Interfaces and Small Particles," *Micron*, Vol. 27, No. 3-4, 265-299, June 1996

[8] Raether, H., *Excitation of Plasmons and Interband Transitions by Electrons.* New York: Springer-Verlag, 1980

[9] Golstein, J. L., et. al, *Scanning Electron Microscopy and X-Ray Microanalysis*, New York: Plenum Press, pg. 57, 1981

[10] G. Ruthemann, Ann. Phys. **6**, 113 (1948)

[11] http://www.dow.com/styron/design/guide/flatplate.htm

[12] Yaniv, Z. and Thuesen, L. H., "The Status of Carbon Electron Emitting Elements Applications," Eurofe2001 Keynote

[13] Mirkin, C., "Programming the Assembly of Two- and Three-Dimensional Architectures with DNA and Nanoscale Inorganic Building Blocks," *Inorganic Chemistry*, Vol. 39, pp. 2258-2272, 2000

[14] Bolton, J. P. R. and Chen, M., "Electron Energy Loss in Multilayered Slabs: I. Normal Incidence," *Journal of Physics. Condensed matter* Vol. 7, pp. 3373-3387, March 1995

[15] http://laser.phys.ualberta.ca/∼egerton/preprint/eels-tut.pdf

[16] Ahn, C. C., Krivanek, O. L., Burgner, R. P., Disko, M. M. and Swann, P. R., *EELS Atlas: A reference collection of electron energy loss spectra covering all stable elements.* Published jointly by ASU HREM Facility and Gatan, Inc., 1983

[17] Aizpurua, J., Classical Electrodynamics Graduate Course Notes, Göteborg, April 1999

[18] Palik, E.D. (ed.) *Handbook of Optical Constants of Solids*, London: Academic Press, Inc. 1985

[19] Wang, Z. L. and Kang, Z. C., *Functional and Smart Materials - Structural Evolution and Structure Analysis*, Plenum Press, pp. 424-429, 1998

[20] Garcia-Molina, R., Gras-Marti, A., Howie, A., and Ritchie, R.H., "Retardation Effects in the Interaction of Charged Particle Beams With Bounded Condensed Media," *Journal of Physics C: Solid State Physics* Vol. 18, pp. 5335-5345, Feb. 1985

[21] Otto, A., "Theory of Plasmon Excitation in Thin Films by Electrons of Non-normal Incidence," *Physica Status Solidi* Vol. 22, pp. 401-406, 1967

[22] Kröger, E., "Transition Radiation, Cernekov Radiation and Energy Losses of Relativistic Charged Particles Traversing Thin Foils at Oblique Incidences," *Zeitschrift für Physik* Vol. 235, pp. 403-421, 1970

[23] Geiger, J., "Inelastic Electron Scattering in Thin Films at Oblique Incidence," *Physics of the Solid State*, Vol. 24, pp. 457-460, 1967

[24] Tougaard, S. and Kraaer, J., "Inelastic-electron-scattering cross sections for Si, Cu, Ag, Au, Ti, Fe, and Pd," *Physical Review B*, Vol. 43, No. 2, pp. 1651-1661, Jan. 1991